2008

Registration-based regional lung mechanical analysis

Kai Ding
University of Iowa

REGISTRATION-BASED REGIONAL LUNG MECHANICAL ANALYSIS

by

Kai Ding

A thesis submitted in partial fulfillment of the
requirements for the Master of Science
degree in Biomedical Engineering
in the Graduate College of
The University of Iowa

August 2008

Thesis Supervisor: Associate Professor Joseph M. Reinhardt

Graduate College
The University of Iowa
Iowa City, Iowa

CERTIFICATE OF APPROVAL

MASTER'S THESIS

This is to certify that the Master's thesis of

Kai Ding

has been approved by the Examining Committee for the thesis requirement for the Master of Science degree in Biomedical Engineering at the August 2008 graduation.

Thesis Committee: _____
Joseph M. Reinhardt, Thesis Supervisor

_____
Gary E. Christensen

_____
Madhavan L. Raghavan

_____
Eric A. Hoffman

_____
Edwin J.R. van Beek

To My Family

ACKNOWLEDGEMENTS

First of all, I would like to thank my parents for their incessant support. Without their help, I would never had the chance to get in touch with the state-of-the-art research, meet the leading scientists in the world and study here at the University of Iowa.

I wish to express my sincere gratitude to Prof. Joseph Reinhardt for his invaluable advice, guidance and support throughout my study. I am greatly indebted to him for his confidence in me, his inspiring and encouraging words and his wealth of brilliant ideas during the research. I appreciate Prof. Xiaoxiang Zheng, my undergraduate thesis advisor, who inspired me to develop interest in the medical imaging field, owing to her experience and expertise. I am grateful to Prof. Gary E. Christensen and his student Kunlin Cao and Joo Hyun Song for help on image registration. Without discussing and consulting with Kunlin Cao, the work could not have proceeded so efficiently. I would like to thank Prof. Eric Hoffman and his student Matthew Fuld for their support and advice in CT imaging and data analysis, and assistance in animal experiments. My special thanks go to Prof. Bram van Ginneken and Keelin Murphy for providing the software iX and assistance in landmark analysis. Thanks to Shalmali Bodas and Matthew Moehlmann for their help for picking landmarks. I would also like to thank Prof. Madhavan Raghavan and Prof. Edwin van Beek for their enlightening talks on biomechanics and functional lung imaging. Thanks to my labmates Sangyeol Lee, Lijun Shi and Sudarshan Bommu for their help and friendship.

The contributions of all these people are greatly appreciated.

This work is supported in part by grant HL079406 from the National Institute of Health.

TABLE OF CONTENTS

LIST OF TABLES vii

LIST OF FIGURES vi

CHAPTER

1 INTRODUCTION 1

1.1 Motivation 1
1.2 The State of the Art 2
1.3 New Approaches 4

2 MATERIALS AND METHODS 5

2.1 Data Acquisition 5
2.1.1 Volumetric CT Data Acquisition by Retrospectively Reconstructed Dynamic Imaging 5
2.1.2 Volumetric CT Data Acquisition by Static Breath-hold Imaging 6
2.1.3 Xenon CT Data Acquisition 6
2.2 Image Registration and Mechanical Analysis 7
2.2.1 The Basics and Problem Modeling 7
2.2.2 Inverse Consistent Image Registration 11
2.2.3 Image Preprocessing and Registration Procedures 14
2.3 Xenon CT and Specific Ventilation 15
2.3.1 Review of Xenon CT Imaging 15
2.3.2 Xenon CT Ventilation Analysis 16
2.4 Quantitative Evaluation of Registration Accuracy 19
2.4.1 Semi-Automatic Reference Standard 19
2.4.2 Manual Reference Standard 22
2.4.3 Comparison between Semi-Automatical and Full-Manual Reference Standards 22
2.5 Comparison between Estimates from Registration and sV 23
2.5.1 Comparison between Estimates of Lung Expansion from Dynamic Scans and sV 23
2.5.2 Comparison between Estimates of Lung Expansion from Static Scans and sV 23

3 RESULTS 25

3.1 Registration Accuracy 25
3.1.1 Landmark Errors from Semi-Automatic Reference Standard 25
3.1.2 Landmark Errors from Manual Reference Standard 28
3.1.3 Comparison of Semi-Automatic and Manual Reference Standards 29
3.2 Regional Lung Expansion and Xe-CT Estimates of sV 31
3.2.1 Estimate of Regional Lung Expansion in Dynamic Scans 32
3.2.2 Estimate of Regional Lung Expansion in Static Scans 35

4 DISCUSSION 37

4.1 Image Registration 37
4.2 Lung Mechanical Changes During Tidal Breathing 39
4.3 Limitations and Future Improvements 40

5 CONCLUSION 44

REFERENCES 46

LIST OF TABLES

3.1 An example of the distance between the automatically matched landmark and the manually matched landmark in differen pressure for animal AS70078. 31

LIST OF FIGURES

2.1 The basic components of the registration framework are two input images, a transform, a cost function, an interpolator and an optimizer. 8

2.2 The gap in the template image, when a forward transform and a reverse transform is applied to a pair of corresponding points. 10

2.3 Color-coded maps showing (a) the Jacobian of the image registration transformation (unitless) for approximately the same anatomic slice computed from the $T0 - T1$ inspiration image pair and (b) the $T4 - T5$ expiration image pair. Note that the color scales are different for (a) and (b). Red regions on the inspiration image (a) are regions that have high expansion while dark blue regions on the expiration image (b) have high contraction. 13

2.4 The intensity transformation maps the CT values to 8-bit unsigned character data before registration. (a) Original CT data. (b) Data after intesity mapping. 15

2.5 Wash-in and wash-out behaviors predicted by compartment model for $t_0 = 5$ seconds, $\tau = 10$ seconds, $D_0 = -620$ HU, and $D_f = -540$ HU. (Figure from [30]) 17

2.6 Time series data from Xe-CT study. (a) shows the Xe-CT image of the lungs, with the lung boundaries marked in blue and a rectangular region of interest in yellow. (b) shows the raw time series data for this region of interest (wash-in phase) and the associated exponential model fit. 18

2.7 An example of image intensity difference before registration which depicts larger difference near the diaphragm than other regions. 20

2.8 An example projection view of all landmarks generated by the algorithm for a scan. 21

2.9 A screen shot of the software system to semi-automatically match hundreds of landmarks. 22

2.10 Example of the result of affine registration between Xe-CT data and dynamic respiratory-gated CT data. (a) $T0$ whole-volume dynamic respiratory-gated CT data. (b) Fused image. (c) Deformed first breath of the Xe-CT data. 24

3.1 Automatically-generated landmark locations projected onto (a) a coronal slice and (b) a sagittal slice for one animal at T0 breathing phase. 25

3.2 Registration accuracy from semi-automatic reference standard by mean ± standard deviation of landmark errors for each phase change pair and for each animal. 26

3.3 Registration accuracy from semi-automatic reference standard by mean ± standard deviation of landmark errors for each pressure change pair and for each animal. 27

3.4 Sagittal view of the landmark position that shows largest registration error in (a) P10 and (b) P15. 27

3.5 Manually-generated landmark locations projected onto (a) a coronal slice and (b) a sagittal slice for one animal at T0 breathing phase. 28

3.6 Registration accuracy by mean ± standard deviation of landmark errors for each phase change pair and for each animal. 29

3.7 Registration accuracy by mean ± standard deviation of landmark errors for each pressure change pair and for each animal. 30

3.8 Landmark error versus lung height for pressure change pair P10 to P15 in animal AS70080. 30

3.9 Color-coded maps showing (a) Jacobian of the registration transformation and (b) specific ventilation (1/min) for approximately the same anatomic slice computed from the $P10 - P15$ image pair of the same sheep. Note that the physical units and color scales are different for (a) and (b). . . . 32

3.10 Example of Jacobian and sV measurements vs. lung height for one animal AS70078. (a) Average Jacobian values for all phase change pairs. (b) Average sV vs. lung height. Lung height equal to 0 cm is the most dorsal position and positive heights move toward the ventral direction. 33

3.11 Examples of scatter plot of average sV and average Jacobian for one animal AS70078 with linear regression with 95% confidence interval for (a) $T0$ to $T1$ phase change pair and (b) $T4$ to $T5$ phase change pair. 34

3.12 Correlation coefficients r^2 from the linear regression of average Jacobian and sV for each phase change pair and for each animal. 35

3.13 Correlation coefficients r^2 from the linear regression of average Jacobian and sV for each pressure change pair and for each animal. 36

4.1 Intensity difference of the lung after inspiration of air. (a) a slice of $P0$ image. (b) a slice of $P10$ image. 39

4.2 Color coded image showing coronal view of the the phase change pair when the largest expansion occurs during inspiration(first row) and the largest contraction occurs during expiration(second row). From left to right: Sheep AS70077, AS70078, AS70079 and AS70080. 41

4.3 Color coded image showing sagittal view of the phase change pair when the largest expansion occurs during inspiration(first row) and the largest contraction occurs during expiration(second row). From left to right: Sheep AS70077, AS70078, AS70079 and AS70080. 41

4.4 An example of the motion hysteresis of a point near diaphragm of sheep AS70078 during tidal breathing. 42

CHAPTER 1
INTRODUCTION

1.1 Motivation

The lungs undergo expansion and contraction during the respiratory cycle. Lung tissue mechanics depends upon the material properties of the lung parenchyma and the relationships between the lungs, diaphragm, and other parts of the respiratory system. Pulmonary diseases can change the tissue material properties of lung parenchyma and the mechanics of the respiratory system. In pulmonary emphysema, a chronic obstructive pulmonary disease (COPD), is characterized by loss of elasticity(increased compliance) of the lung tissue, from destruction of structures supporting the alveoli and destruction of capillaries feeding the alveoli [29]. Idiopathic pulmonary fibrosis (IPF), a classic interstitial lung disease, causes inflammation and fibrosis of tissue in the lungs. Over time, the disease makes the tissue thicker and stiffer (reduced compliance). While these mechanical changes associated with the change of the material properties (and the disease process itself) originate at a regional level, they are largely asymptomatic and invisible to currently available global measures of lung function such as pulmonary function tests (PFTs) until they have significantly advanced and aggregated. Therefore it would be desirable to have objective methods with which to determine the stage and follow the progression of the disease from regional measurements. Recent advances in multidetector-row CT (MDCT) allow the entire lung to be imaged with isotropic 0.4 mm voxels in under 10 seconds. Additionally, new retrospective gating methods, initially used to reconstruct the beating heart, are being applied to produce high-resolution images of the entire breathing

lung throughout the respiratory cycle. These dynamic imaging capabilities now permit the measurement of regional lung mechanical properties which, in addition with recently established functional CT tools for measurement of regional lung ventilation [25, 36] and perfusion [41], will greatly enhance the quantitative characterization of lung structure and function.

1.2 The State of the Art

Various efforts have been made to assess lung function. Invasive methods, such as percutaneously or surgically implanted parenchymal markers or inhaled fluorescent microspheres, are not possible for translation to humans [15, 18, 31]. Nuclear medicine imaging such as positron emission tomography (PET) and single photon emission CT (SPECT) can provide an assessment of lung function [23], but its application is constrained by low spatial resolution in pulmonary imaging when images are acquired across several respiratory cycles. Venegas et al. have used PET to study patchiness in asthma [39]. However the experiments were limited to 6.5mm slice thickness and 10cm axial coverage. Standard CT, on the other hand, has been the main diagnostic modality for evaluation of lung diseases and can provide high-resolution images but it is largely static and does not provide ventilation assessment. Hyperpolarized noble gas MR imaging has been developed for functional imaging of pulmonary ventilation [27, 38, 16]. Most common marker gases for lung studies are helium (He^3), xenon (Xe^{129}) and fluorene (F^{19}). Another method for the assessment of regional ventilation by MRI is the use of oxygen for signal enhancement. The signal from paramagnetic O_2 is inferior to that from spin-polarized He^3, but the method is method is less complex and provides clinically useful information. Although MR

imaging avoids the concern about ionizing radiation, there is insufficient signal from airway walls to visualize anything but the largest airways. Finally, the other imaging modality to directly assess lung function is the xenon-enhanced CT (Xe-CT) which measures regional ventilation by observing the gas wash-in and wash-out rate on serial CT images [25, 36, 4]. However, Xe-CT also has some shortcomings. Compared with standard CT, it involves inhalation of stable Xenon by the patient, with possible side effects, and necessitates expensive and complex equipment, available only in few medical centers. Xe-CT imaging protocols require high temporal resolution imaging, so axial coverage is usually limited. Z-axis coverage with modern multi-detector scanners currently ranges from about 2.5 to 12 cm, but the typical z-axis extent of the human lung is on the order of 25 cm. While developing pulmonary imaging techniques to assess lung function is attracting great interests of research, recently, investigators from other groups have studied the lung function in the perspective of lung mechanics. Guerrero et al. have used optical-flow registration to compute lung ventilation from 4D CT [14, 13]. Gee et al. have used non-rigid registration to study pulmonary kinematics [11, 35] using magnetic resonance imaging. Christensen et al. used image registration to match images across cine-CT sequences and estimate rates of local tissue expansion and contraction [5] and their measurements matched well with spirometry data. While they were able to show that their accumulated measurement matched well with the global measurement, they were not able to compare the registration-based measurements to local measures of regional tissue ventilation. In other words, they were not able to validate their methods at regional level to show the linkage between lung mechanics and lung function.

1.3 New Approaches

We describe a technique that uses multiple respiratory-gated CT images of the lung acquired at different levels of inflation with both breath-hold static imaging and retrospectively reconstructed dynamic imaging, along with non-rigid 3D image registration, to make local estimates of lung tissue expansion. We not only compare these lung expansion estimates to Xe-CT derived measures of regional ventilation to validate our measurements and establish their physiological significance, but also apply the semi-automatic reference standard to quantitatively evaluate the accuracy of 3D image registration. The ability to estimate regional expansion maps as a surrogate of the Xe-CT ventilation imaging for the entire lung from quickly and easily obtained respiratory-gated images, is a significant contribution to functional lung imaging because of the potential increase in resolution, and large reductions in imaging time, radiation, and contrast agent exposure.

The next of the thesis will describe our methods of applying the Xe-CT imaging, non-rigid 3D image registration, and semi-automatic reference standard in great details at chapter 2. And the review of each technique will also be provided whenever necessary. In chapter 3, we will show that the lung expansion estimates by 3D image registration match equally well with the Xe-CT derived measures of regional ventilation in both breath-hold static imaging and retrospectively reconstructed dynamic imaging. The quantitative evaluation of the registration accuracy further confirm our results. We also discuss the related unsolved problems in our methods and future work in the chapter 4.

CHAPTER 2
MATERIALS AND METHODS

2.1 Data Acquisition

Appropriate animal ethics approval was obtained for these protocols from the University of Iowa Animal Care and Use Committee and the study adhered to NIH guidelines for animal experimentation. Four adult sheep were used for experiments. The sheep were anesthetized using intravenous pentobarbital and mechanically ventilated during experiments. All images were acquired with the animals in the supine orientation on a Siemens Sensation 64 multi-detector CT scanner (MDCT) (Siemens Medical Solutions; Erlangen, Germany).

2.1.1 Volumetric CT Data Acquisition by Retrospectively Reconstructed Dynamic Imaging

The dynamic scans are acquired using the dynamic imaging protocol during tidal breathing with a pitch of 0.1 , slice collimation 0.6 mm, rotation time 0.5 sec, slice thickness 0.75 mm, increment 0.5 mm, 120 kV, 400 mAs, and kernel B30f. Images are reconstructed retrospectively at 0, 25, 50, 75, and 100% phase points of the inspiratory portion and 75, 50 and 25% of the expiration portion of the respiratory cycle(herein denoted as the $T0$, $T1$, $T2$, $T3$, $T4$, $T5$, $T6$, and $T7$ images).

2.1.2 Volumetric CT Data Acquisition by Static Breath-hold Imaging

The static scans are acquired in static imaging protocol at 10, 15, 20, and 25 cm H_2O (herein denoted as the $P10$, $P15$, $P20$, and $P25$ images) airway pressure with the animal held apneic. The protocol used a tube current of 100 mAs, a tube voltage 120 kV, slice collimation of 0.6 mm, an effective slice thickness of 0.75 mm, a slice separation of 0.5 mm, a pitch of 1, and a field of view selected to fit the lung field of interest. Both of the two types of scans are acquired with a reconstruction matrix of 512 by 512 and without moving the animal between scans, so after acquisition the data sets are in rigid alignment.

2.1.3 Xenon CT Data Acquisition

The axial locations for the Xe-CT studies are selected from the whole lung volumetric scan performed near end-expiration. Images are acquired with the scanner set in ventilation triggering mode, typically using 80 keV energy for higher Xe signal enhancement (as shown in pilot study [3]), 160 mAs tube current, a 360° rotation, a 0.33 sec scan time, a 512 by 512 reconstruction matrix, and a field of view adjusted to fit the lung field of interest. The Xe-CT slice thickness is approximately 2.4 mm thick, or about 3.4 times thicker than the volumetric CT slices. Twelve contiguous xenon slices are acquired and provide approximately 3 cm of coverage along the axial direction. Respiratory gating during image acquisition is achieved by replacing the standard ECG gating signal with a trigger signal from a LabView program. Images were acquired at the end expiratory point during the respiratory cycle. A respiratory tidal volume of 8 cc/kg was used for the Xe-CT acquisition.

The image acquisition sequence is as follows. Acquisition starts and images are gathered as the animal breathes six to eight breaths of room air. Next, the xenon delivery system is turned on and approximately 40 breaths of pure xenon are delivered while imaging, and then the air source is switched back to room air for another 40 breaths. Thus, axial images are acquired for approximately 90 breaths as the xenon gas washes in and out of the lungs.

2.2 Image Registration and Mechanical Analysis

2.2.1 The Basics and Problem Modeling

In order to study lung mechanics, we wish to find the movement of all matter inside the lung due to the interactions with each other caused by the change of the transpulmonary pressure. The movement of the matter inside the lung, or lung tissue, can be expressed in the form of spatial function of each region of the lung if the mapping of the region between different conditions can be found. Therefore, the problem can be stated as: Given images of the lungs in two or more different conditions, find the region correspondences between the different conditions.

The problem statement brings us into the realm of image registration. Image registration is the task of finding a spatial transform mapping on image into another. Many image registration algorithms have been proposed and various of features such as landmarks, contours, surfaces and volumes have been utilized to manually, semi-automatically or automatically define correspondences between two images [24, 22]. The basic components of the registration frame and their interconnections are shown in Figure 2.1 [19, 9]. The basic input data to the registration process are two images:

one is defined as the *moving* or *template* image $I_t(\mathbf{X})$ and the other as the *fixed* or *target* image $I_s(\mathbf{X})$, where $\mathbf{X}$ represents a position in N-dimensional space. The registration is treated as an optimization problem with the goal of finding the spatial mapping that brings the features of the moving template image into alignment with the fixed target image.

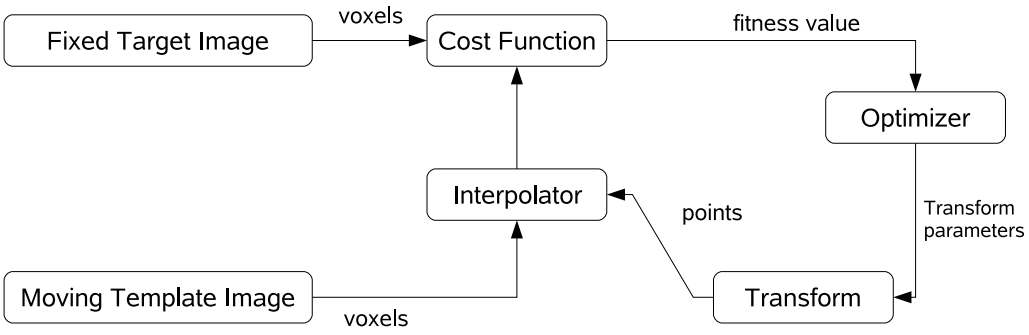

Figure 2.1: The basic components of the registration framework are two input images, a transform, a cost function, an interpolator and an optimizer.

The transformation component h defines how one image can be deformed to match another. It can be a simple rigid or affine transformation which can be described very compactly between 6 (3 translations and 3 rotations) and 12 (6 + 3 scalings + 3 shears) parameters for a whole image, or non-rigid registration such as the spline-based registrations, elastic models, fluid models, finite element (FE) models etc. The interpolator is used to evaluate the template image intensities at non-rigid positions.

The cost function component can consist of a single metric such as a similarity measure based on geometric and intensity approaches or a compound function with

other regulations and constraints depending on potential models. It measures how well the fixed target image is matched by the transformed moving template image. This function forms the quantitative criterion to be optimized by the optimizer over the search space defined by the parameters of the transform. Most registration algorithms can employ standard optimization ways to solve the problems to find the good transformation and there are several existing methods in numerical analysis such as the partial differential equation(PDE) solvers to solve the elastic and fluid transformation, Steepest Gradient Descent, the Conjugate Gradient Method etc.

It is very important to design the ideal cost function and the registration model, since they largely affect the registration result and the time cost of the optimization. The ideal cost function and registration model should be application oriented. For example, the elastic model treat the image as a linear, elastic solid and deform it using forces derived from an image similarity measure. Because of the assumption of linear elasticity, it is only applicable to small deformations and is hard to recover large image difference. In contrast, the viscous fluid model allows large deformations and greater flexibility but with the higher risks of mismatching.

Last, but not the least, is the validation of the registration algorithm. It is used to prove that the algorithm can be applied to a specific task with acceptable errors depending on the task itself. It is usually done by the methods of analyzing the distance of the corresponding landmarks before and after registration. Though this method can estimate well the errors of rigid-registration, it cannot represent all the regions in the non-rigid registration. The validation of registration will be described in the following subsections in more detail.

It is also worth to notice that typically the transformation is asymmetric: al-

though there will be a vector that describes how to displace each point in the template image to find the corresponding location in the target image, there is no guarantee that, at the same scale, each point in the target image can be related to a corresponding position in the template image. There may be gaps in the template image where correspondence is not defined at the selected scale. However, it is necessary to avoid these gaps since they may introduce ambiguity if our region of interest has been identified at different conditions. For example, as shown in Figure 2.2, we cannot confirm which vessel region we are interested if we track same anatomical structure of the vessel from the template image to the target image and the other way around.

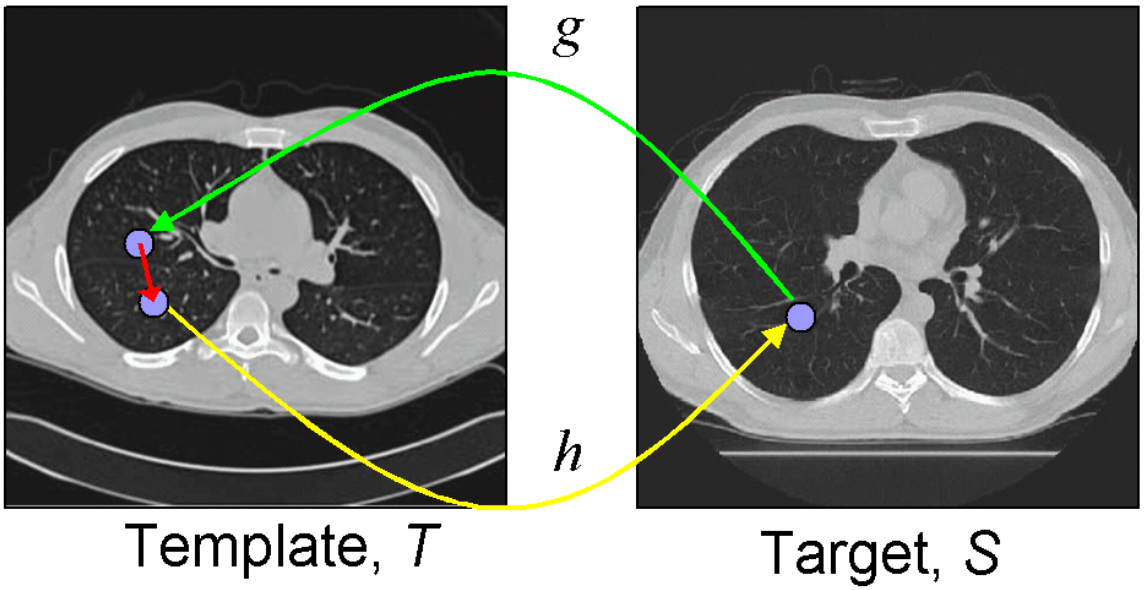

Figure 2.2: The gap in the template image, when a forward transform and a reverse transform is applied to a pair of corresponding points.

In other words, the registration algorithms can be used to determine the spatial locations of corresponding voxels in a sequence of pulmonary scans. The computed

correspondences immediately yield the displacement fields corresponding with the motion of the lung between a pair of images.

Our problem now remains in to find an ideal registration algorithm that best describes the transform of the regions of the lung between different conditions. Based on the assumptions that lung is an elastic body and that the requirements of our study that a specific region should be able to be trackable across different conditions without ambiguity, we introduce the inverse consistent registration algorithm which is inherently armed with these two features.

2.2.2 Inverse Consistent Image Registration

Inverse consistent linear elastic image registration was applied to register image pairs [6]. The registration estimates the inverse consistency error between the forward and reverse transformation, and hence provides more accurate correspondences between two images compared to independent forward and reverse transformations. Let the two input images of the registration be denoted as I_0 and I_1, and let the transforms between two images be h and g. The forward transformation h is used to deform the image I_0 into the shape of the image I_1, and the reverse transformation g is used to deform the shape of I_1 into that of I_0. The deformed template and target images are denoted by $(I_0 \circ h)$ and $(I_1 \circ g)$, respectively. The forward and reverse transformations are defined by the equations: $h(\mathbf{X}) = \mathbf{X} + u(\mathbf{X})$, $g(\mathbf{X}) = \mathbf{X} + w(\mathbf{X})$, $h^{-1}(\mathbf{X}) = \mathbf{X} + \tilde{u}(\mathbf{X})$, $g^{-1}(\mathbf{X}) = \mathbf{X} + \tilde{w}(\mathbf{X})$. The vector-valued functions u, w, $\tilde{u}$, and $\tilde{w}$ are called displacement fields since they define the transformation in terms of a displacement from a location $\mathbf{X}$.

The registration minimizes the cost function defined as:

$$\begin{aligned} C &= \sigma[C_{SIM}(I_0 \circ h, I_1) + C_{SIM}(I_1 \circ g, I_0)] + \\ &\chi[C_{ICC}(u, \tilde{w}) + C_{ICC}(w, \tilde{u})] + \\ &\rho[C_{REG}(u) + C_{REG}(w)], \end{aligned} \tag{2.1}$$

The C_{SIM} term of the cost function defines the symmetric intensity similarity. The C_{ICC} term is the inverse consistency constraint or inverse consistency error cost and is minimized when the forward and reverse transformations are inverses of each other. The C_{REG} term is used to regularize the forward and reverse displacement fields. A 3D Fourier series representation [1] is used to parameterize the forward and reverse transformations. Christensen and Johnson [6, 20] describe the Fourier series parameterization used in the consistent registration algorithm in detail. The constants σ, χ and ρ are used to enforce/balance the constraints. In our registrations, the mean squared intensity difference is used as similarity measure to drive the registration, and we set the weighting constants $\sigma = 1$, $\chi = 600$, and $\rho = 0.00125$. The parameters were decided on the basis of pilot experiments, previous work and experience. The forward and reverse transformations are parameterized using Fourier series representation and the gradient descent is used in the optimization step. More details of the inverse consistent registration can be found in [6, 21].

After finding out the transforms and the correspondence for each voxel of two images, we are ready for mechanical analysis on a regional level. In three-dimensional space, the vector displacement function $\vec{u}(x, y, z)$ that maps image I_0 to image I_1 is

used to calculate the local lung expansion using the Jacobian determinant $J(x, y, z)$ defined as:

$$J(x,y,z) = \begin{vmatrix} 1+\frac{\partial u_x(x,y,z)}{\partial x} & \frac{\partial u_x(x,y,z)}{\partial y} & \frac{\partial u_x(x,y,z)}{\partial z} \\ \frac{\partial u_y(x,y,z)}{\partial x} & 1+\frac{\partial u_y(x,y,z)}{\partial y} & \frac{\partial u_y(x,y,z)}{\partial z} \\ \frac{\partial u_z(x,y,z)}{\partial x} & \frac{\partial u_z(x,y,z)}{\partial y} & 1+\frac{\partial u_z(x,y,z)}{\partial z} \end{vmatrix},$$

where $u_x(x, y, z)$ is the x component of $\vec{u}(x, y, z)$, $u_y(x, y, z)$ is the y component of $\vec{u}(x, y, z)$, and $u_z(x, y, z)$ is the z component of $\vec{u}(x, y, z)$.

The Jacobian measures the differential expansion at position (x, y, z) in the image I_1. If the Jacobian is greater than one, there is local tissue expansion; if the Jacobian is less than one, there is local tissue contraction (Figure 2.3).

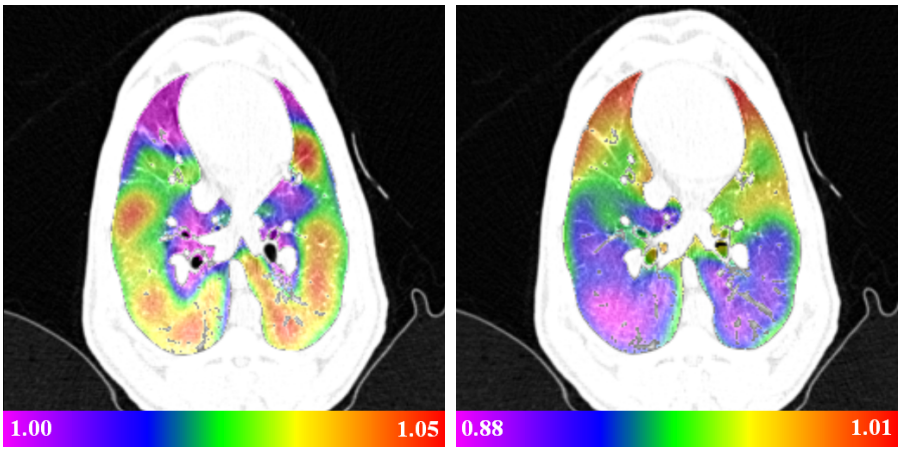

(a) (b)

Figure 2.3: Color-coded maps showing (a) the Jacobian of the image registration transformation (unitless) for approximately the same anatomic slice computed from the $T0 - T1$ inspiration image pair and (b) the $T4 - T5$ expiration image pair. Note that the color scales are different for (a) and (b). Red regions on the inspiration image (a) are regions that have high expansion while dark blue regions on the expiration image (b) have high contraction.

2.2.3 Image Preprocessing and Registration Procedures

All volumetric CT data were converted from DICOM format and stored in 16-bit Analyze^{TM} (Mayo Clinic, Rochester, MN) format. To reduce memory requirements during the image registration and increase the image contrast, the original 16-bit CT data were then converted to 8-bit values [0, 255] using a threshold window of [-1024HU, 0HU]. The intensity discontinuity at the boundary along the chest wall and the large intensity difference between the regions inside and outside the lung increase the mean squared intensity difference of our similarity measure and thus the total cost function, if the regions are misaligned at boundaries. In this way, the boundaries of each region are forced to match. Yet the matching does not constrain the sliding motion between the lungs and the ribs along the boundary at different pressure or phases(Figure 2.4)

As described Section 2.2.2, the inverse consistent registration algorithm uses Fourier series representation to parameterize the transformations, so it requires the sizes of the input images to be a power of two. Therefore the images are padded with zeros to size $512 \times 512 \times 2^{\text{round}(\log_2 N_z)}$, where N_z is the size of the image in Z-direction. Then to reduce the memory requirements, the images are downsampled by a factor of two in all three directions using trilinear interpolation.

Since both of the dynamic and static scans are acquired without moving the animal between scans, and after acquisition the data sets are in rigid alignment, so the common rigid registration step to initially align two images as seen in other papers is not performed.

In our study, inverse consistent image registration followed by regional me-

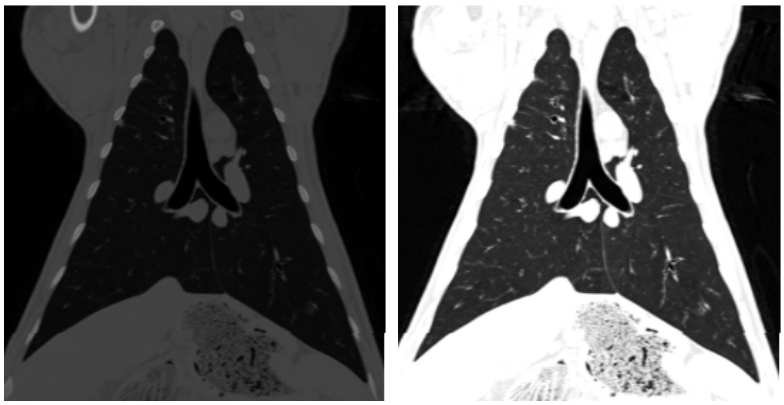

(a) (b)

Figure 2.4: The intensity transformation maps the CT values to 8-bit unsigned character data before registration. (a) Original CT data. (b) Data after intesity mapping.

chanical analysis as described in Section 2.2.2 is performed for $T0$ to $T1$, $T1$ to $T2$, ..., and $T6$ to $T7$ in the dynamic scans and for $P10$ to $P15$, $P15$ to $P20$ and $P20$ to $P25$ in the static scans.

2.3 Xenon CT and Specific Ventilation

2.3.1 Review of Xenon CT Imaging

Xe-enhanced computed tomography (CT; Xe-CT) is a method for the noninvasive measurement of regional pulmonary ventilation in intact subjects [34, 25, 36]. Xenon is a nonradioactive, monatomic noble gas that is denser than air. When imaged in a conventional CT scanner, the density of Xe measured in Hounsfield units (HU) increases linearly with its concentration. When Xe concentrations of 30-60% in air are delivered to the lung, CT enhancements of parenchymal density of 50-150 HU are obtained. If the Xe is introduced and eliminated from the lung during a controlled washin-washout (wi/wo) ventilation protocol, repeat CT scans taken at constant lung volume (i.e., at the same point in the respiratory cycle) will yield a

local exponential density curve for any specified region of interest (ROI)within the lung field. The regional ventilation can be quantified by fitting a single-compartment exponential model to the rise and decay portions of the curve using a least-squares fit. For each ROI to be analyzed, the mean region density, $D(t)$, is calculated versus time (or equivalently, image number). For the wash-in phase, the compartment model gives [34]:

$$D(t) = \begin{cases} D_0 & 0 \leq t < t_0 \\ D_0 + (D_f - D_0)(1 - e^{-\frac{t-t_0}{\tau}}) & t \geq t_0, \end{cases} \tag{2.2}$$

where D_0 is the baseline density in the ROI prior to switching to xenon gas, D_f is the density that would be observed if xenon was inspired until equilibrium, t_0 is the start time of the switchover from room air to xenon, and τ is the model time constant. Thus, using this model, the $D_f - D_0$ term represents the enhancement due to the inspired xenon. The model gives a similar expression for the wash-out phase:

$$D(t) = \begin{cases} D_f & 0 \leq t < t_0 \\ D_0 + (D_f - D_0)e^{-\frac{t-t_0}{\tau}} & t \geq t_0, \end{cases} \tag{2.3}$$

where for the wash-out phase t_0 denotes the time of switchover from xenon back to room air. Figure 2.5 shows the density–time variation predicted by the model.

2.3.2 Xenon CT Ventilation Analysis

Prior to Xe-CT data analysis, the lung region was defined using the method from [17], followed, when necessary, by manual editing. Figure 2.6a shows an example Xe-CT slice with the lung segmentation overlaid. After lung segmentation, non-overlapping 8×8 pixel regions of interest (ROIs) were defined in the lung region on

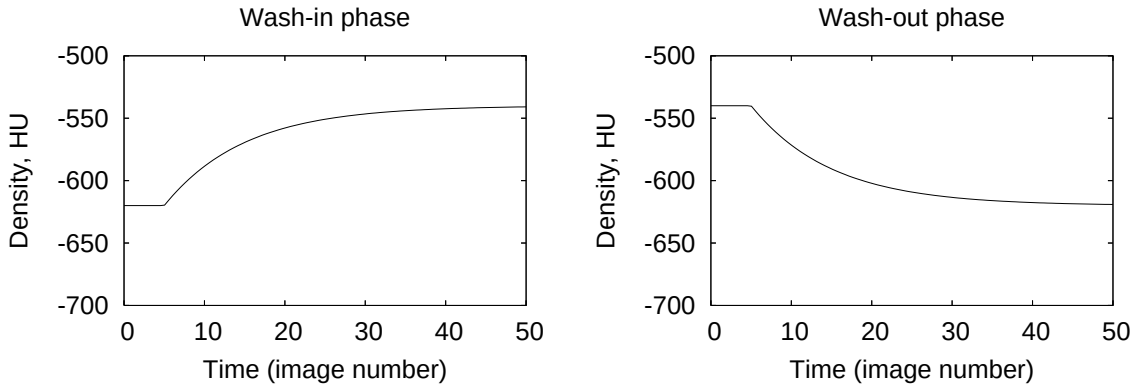

(a) (b)

Figure 2.5: Wash-in and wash-out behaviors predicted by compartment model for $t_0 = 5$ seconds, $\tau = 10$ seconds, $D_0 = -620$ HU, and $D_f = -540$ HU. (Figure from [30])

each 2D slice.

As discussed by [4], the time constants of the rising and falling phases of the curves may be fitted separately or may be forced to be equal. In our analysis, only the wash-in phase of the Xe protocol was analyzed. To reduce aberrations in the time series data due to the ROIs overlapping with large blood vessels or regions of atelectasis (see, for example, the bottom left side of the lungs shown in Figure 2.6a), we eliminated from consideration any ROI that had more than 40% of its pixels above -300 HU. Time series data was measured and analyzed for the remaining ROIs. Specific ventilation (sV, ventilation per unit lung air volume in min^{-1}) for each ROI was calculated as the inverse of the time constant τ.

Figures 2.6a–b shows screen shots from the software tool "time-series image analysis" (TSIA) used to analyze the Xe-CT data [4]. This tool facilitates lung segmentation, region of interest specification, and allows control over the curve fitting parameters during the exponential fits.

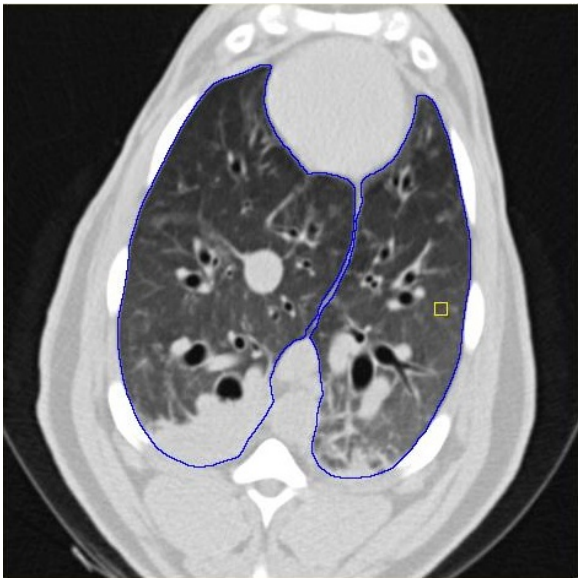

(a)

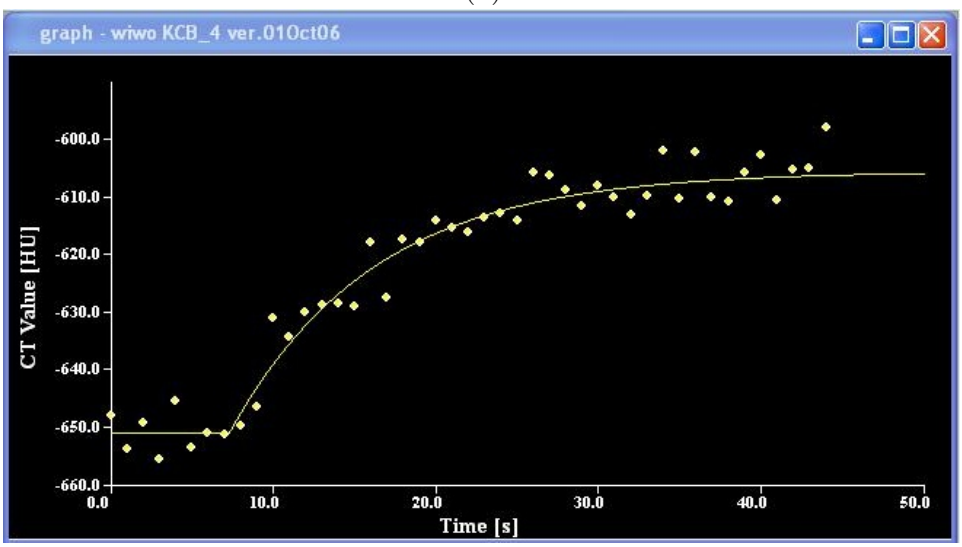

(b)

Figure 2.6: Time series data from Xe-CT study. (a) shows the Xe-CT image of the lungs, with the lung boundaries marked in blue and a rectangular region of interest in yellow. (b) shows the raw time series data for this region of interest (wash-in phase) and the associated exponential model fit.

2.4 Quantitative Evaluation of Registration Accuracy

Although registration result can be assessed by visual comparison, it is highly desired to have quantitative evaluation of registration accuracy. An attempt has been made to establish the registration reference by synthetically warping data such that the original image and the transformed image are known in advance as well as the ideal transform between them [37]. However, this approach provides only a generic evaluation and algorithm performance on real clinical data cannot be measure in this way. In [30], we measured the registration accuracy based on small numbers of manually annotated landmarks position which provide information about the registration quality at only a small number of manually selected locations at airway branches. While the airway branchpoints can be easily recognized by trained observer, the mean movement of the airway branchpoints cannot represent the movement of parenchyma in other regions which have larger movement during respiration. It is our interest to know how the algorithm performs in the regions where large deformation appears, such as the regions near diaphragm (Figure 2.7).

2.4.1 Semi-Automatic Reference Standard

Automatic landmark detection algorithm [28] was applied to find and match the landmarks across the static scans and the dynamic scans. The algorithm automatically detects "Distinctive" points in the fixed image as the landmarks based on the distinctiveness value $D(p)$. Around each point p, 45 points, $q_1 ... q_{45}$ are uniformly distributed on a spherical surface with a radius of 8 voxels. A region of interest $ROI(q_i)$ is compared with the corresponding region of interest $ROI(p)$ around the

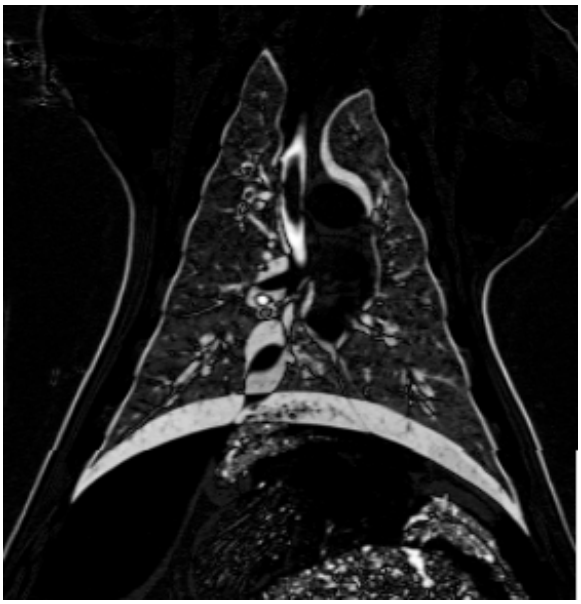

Figure 2.7: An example of image intensity difference before registration which depicts larger difference near the diaphragm than other regions.

original point p. $D(p)$ is calculated as:

$$D(p) = \frac{G(p)}{max_j(G(p_j))} \sum_{i=1}^{45} \frac{\text{Diff}(ROI(p), ROI(q_i))}{45} \tag{2.4}$$

where $G(p)$ is the gradient value of point $p_(x, y, z)$, j is the total number of the landmarks we intend to have and $\text{Diff}(ROI(p), ROI(q_i))$ is the average difference of the voxel intensities in the two ROIs.

Figure 2.8 shows an example projection view of all landmarks generated by the algorithm for a scan.

A semi-automatic system [28] is then applied to guide the observer to find the landmarks in the fixed image with their corresponding voxels in the moving image. Each landmark-pair manually annotated by the observer is added to a thin-plate-spline to warp the moving image. The system utilize the warped image to estimate

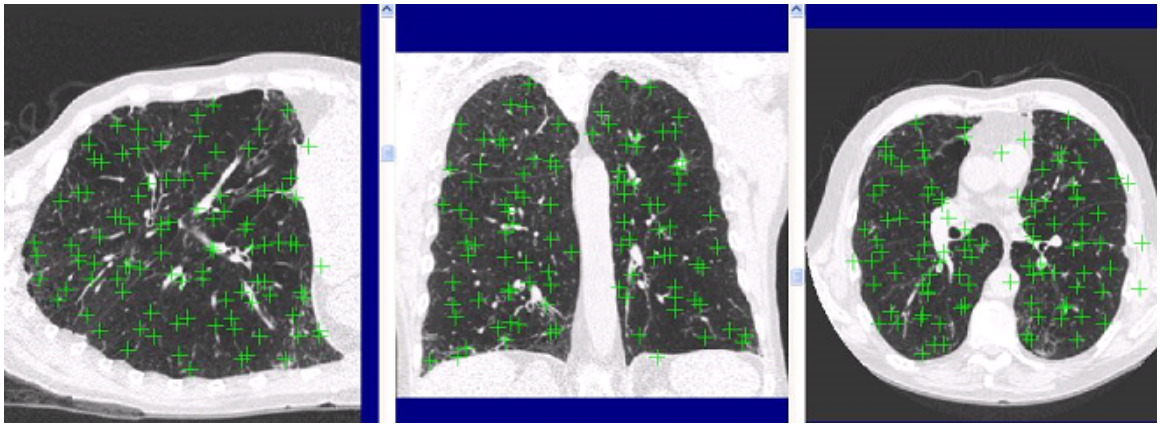

Figure 2.8: An example projection view of all landmarks generated by the algorithm for a scan.

where the anatomic match will be located for a new landmark point presented to the observer, therefore the observer can start the matching from a system estimated location. Thus, as the warped image becomes more accurate by the new added landmarks, the task of the observer and becomes easy. The system will calculate the automatic point correspondence for the rest of the landmarks if the user has successfully marked 30 landmarks fully manually and the computer has predicted at least 10 correspondences in a row correctly. Screen shots from the system are shown in Figure 2.9.

For each animal, after 200 anatomic landmarks are identified in the static scan $P10$ and dynamic scan $T0$, the observer marked the locations of the voxels corresponding to the anatomic locations of the landmarks in the rest static or dynamic scans. For each landmark, the actual landmark position was compared to the registration-derived estimate of landmark position and the error was calculated.

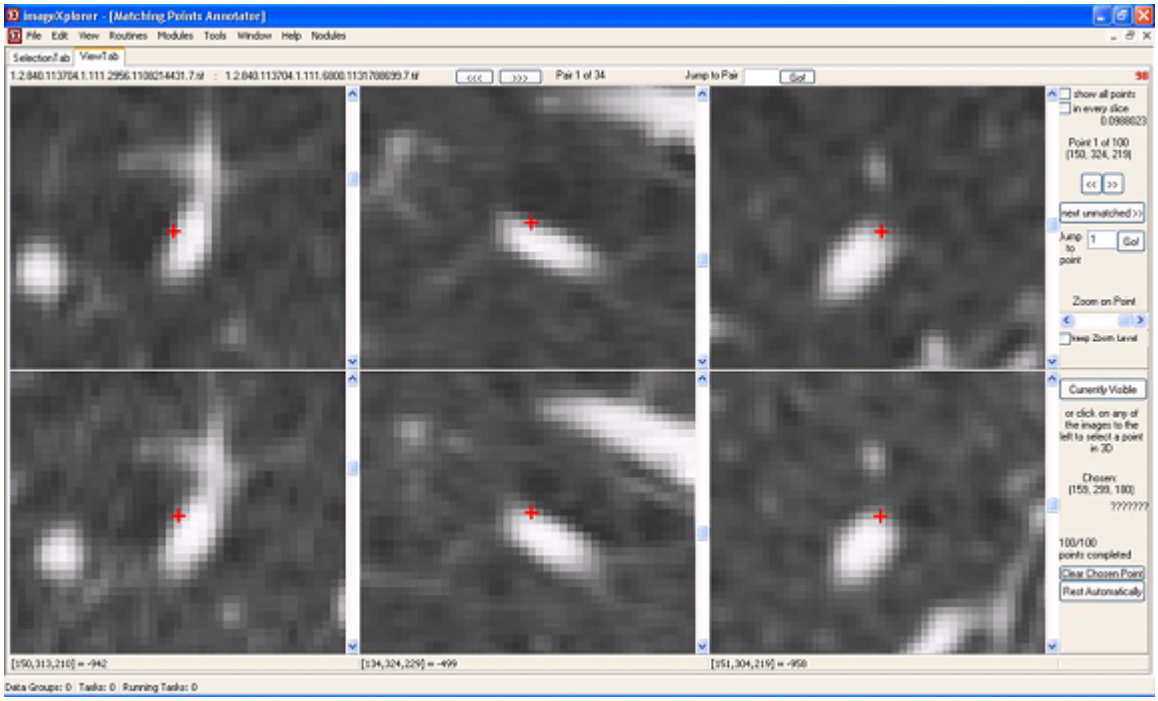

Figure 2.9: A screen shot of the software system to semi-automatically match hundreds of landmarks.

2.4.2 Manual Reference Standard

For each animal, 20 anatomic landmarks were also manually selected and matched between all four static scans $P10, \ldots, P25$ and all eight dynamic scans $T0, \ldots, T7$. The selected landmarks were recognizable branchpoints of the airway branches. For each landmark, the actual landmark position was compared to the registration-derived estimate of landmark position and the error was calculated.

2.4.3 Comparison between Semi-Automatical and Full-Manual Reference Standards

The estimates of the registration accuracy by both methods were compared. In addition, in order to compare performance of automatic points calculation of the system, 20 anatomic landmarks picked manually at the airway branchpoints were also

matched automatically across scans.

2.5 Comparison between Estimates from Registration and sV

2.5.1 Comparison between Estimates of Lung Expansion from Dynamic Scans and sV

To compare the Jacobian values with the sV, we must identify corresponding regions in the two images. The Xe-CT has only twelve slices of axial coverage and the data sets are acquired in rigid alignment as described in Section 2.1, so we register the twelve-slice Xe-CT data to the $T0$ whole-volume retrospectively reconstructed dynamic CT data using rigid affine registration as shown in Figure 2.10. We subdivide the Xe-CT data into around 30 slabs along the y (ventral–dorsal) axis. We track the deformation of each slab across the sequence of volume images (i.e., from $T0$ to $T1$, $T1$ to $T2$ and etc.) and compare the average Jacobian within each slab to the corresponding average sV measurement in the Xe-CT images in the manner of correlation coefficient by linear regression.

2.5.2 Comparison between Estimates of Lung Expansion from Static Scans and sV

Similarly, we first register the twelve-slice Xe-CT data to the $P10$ whole-volume breath-hold static CT data using same rigid affine registration. The lung region corresponding to the Xe-CT image in the static scan is divided into slabs and the motion of each slab can be tracked using resulting displacement fields. Then

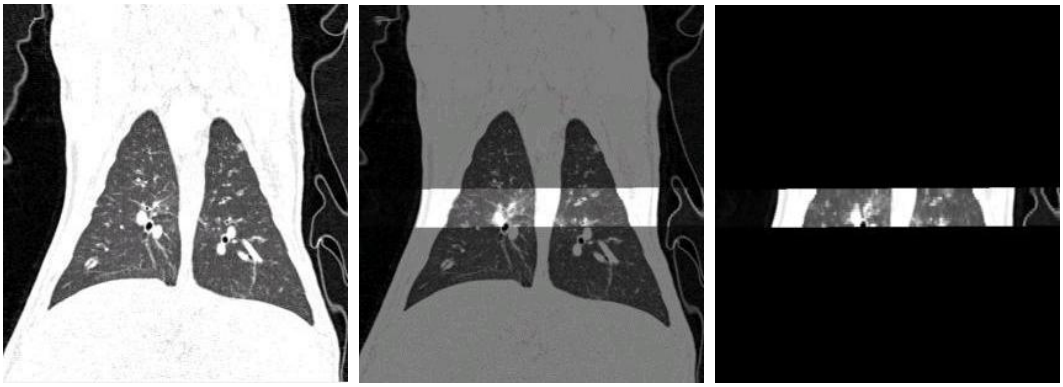

(a) (b) (c)

Figure 2.10: Example of the result of affine registration between Xe-CT data and dynamic respiratory-gated CT data. (a) $T0$ whole-volume dynamic respiratory-gated CT data. (b) Fused image. (c) Deformed first breath of the Xe-CT data.

the average Jacobian in each slab is compared with the average sV. The correlation coefficients between the two estimates are calculated by linear regression.

It is worth noticing that because of the different data acquisition methods of the dynamic scans, static scans and Xe-CT data, the correlation coefficient may be affected by different breathing pattern. For example, the Xe-CT data and the dynamic scans are all acquired when the animals are during tidal breathing while the static data is acquired at discrete breath-hold pressures.

CHAPTER 3
RESULTS

3.1 Registration Accuracy

3.1.1 Landmark Errors

from Semi-Automatic Reference Standard

In our study, 200 landmarks were automatically generated by the algorithm described in Section 2.4.1. Figure 3.1 a and b shows the projection of the automatically-generated landmark locations onto coronal and sagittal slices for one animal. This figure shows that landmarks are distributed widely inside the lung.

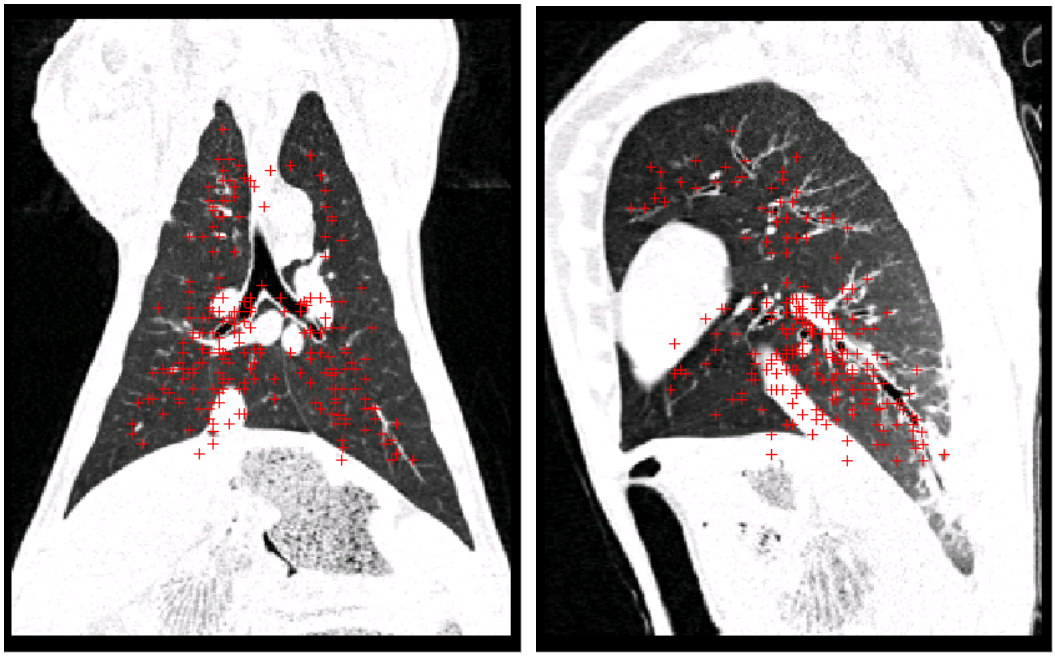

(a) (b)

Figure 3.1: Automatically-generated landmark locations projected onto (a) a coronal slice and (b) a sagittal slice for one animal at T0 breathing phase.

Figure 3.2 shows the registration accuracy as assessed by predicting the motion of the 200 automatically generated landmarks across seven phase change pairs. Overall the registration accuracy is on the order of 1 mm, or about 2 voxels.

Figure 3.3 shows the registration accuracy as assessed by predicting the motion of the 200 automatically generated landmarks across three pressure change pairs. It can be noticed that the registration error is abnormally large for pressure change pair P10 to P15 for animal AS70078. After further inspection, it is observed that the large registration error is caused by the poor contrast in most of the dorsal region where the animal may have atelectasis. It is shown in Figure 3.4, in which the location of the cross is the position of the landmark that shows largest registration error (9mm).

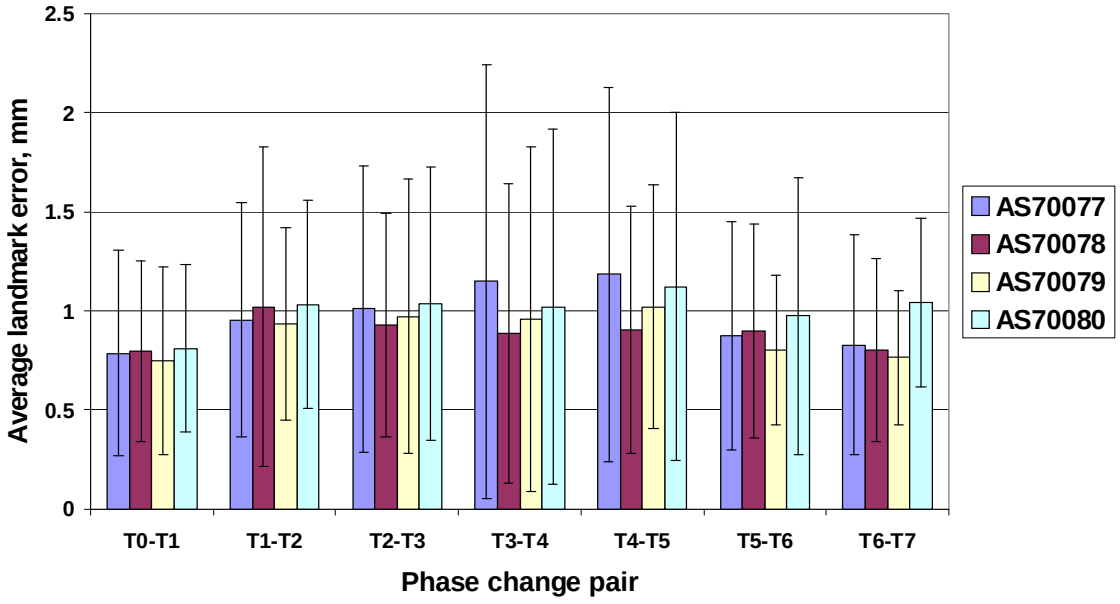

Figure 3.2: Registration accuracy from semi-automatic reference standard by mean ± standard deviation of landmark errors for each phase change pair and for each animal.

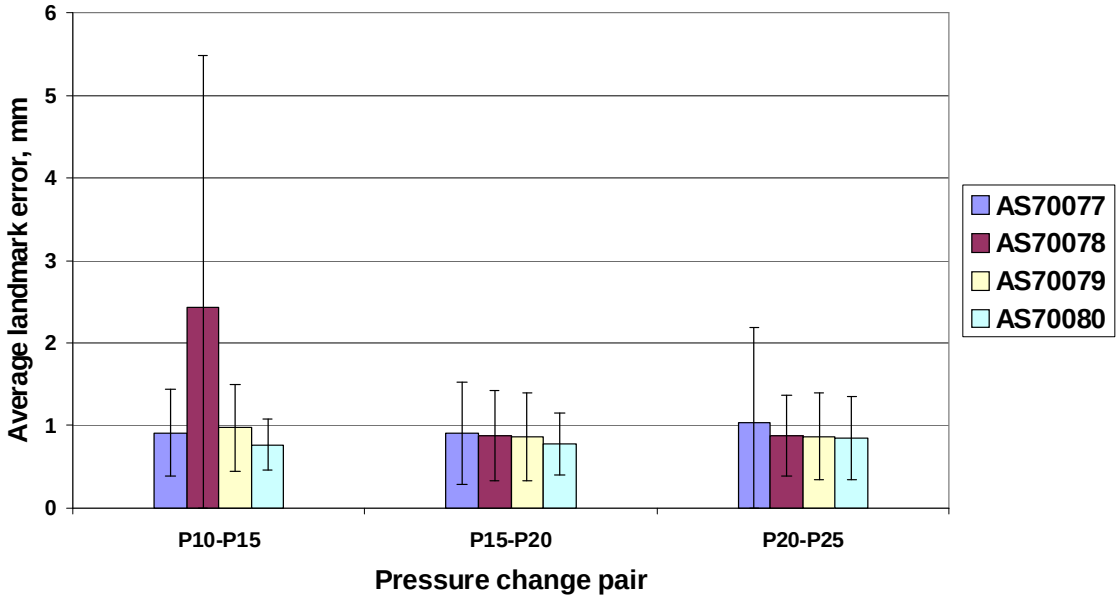

Figure 3.3: Registration accuracy from semi-automatic reference standard by mean ± standard deviation of landmark errors for each pressure change pair and for each animal.

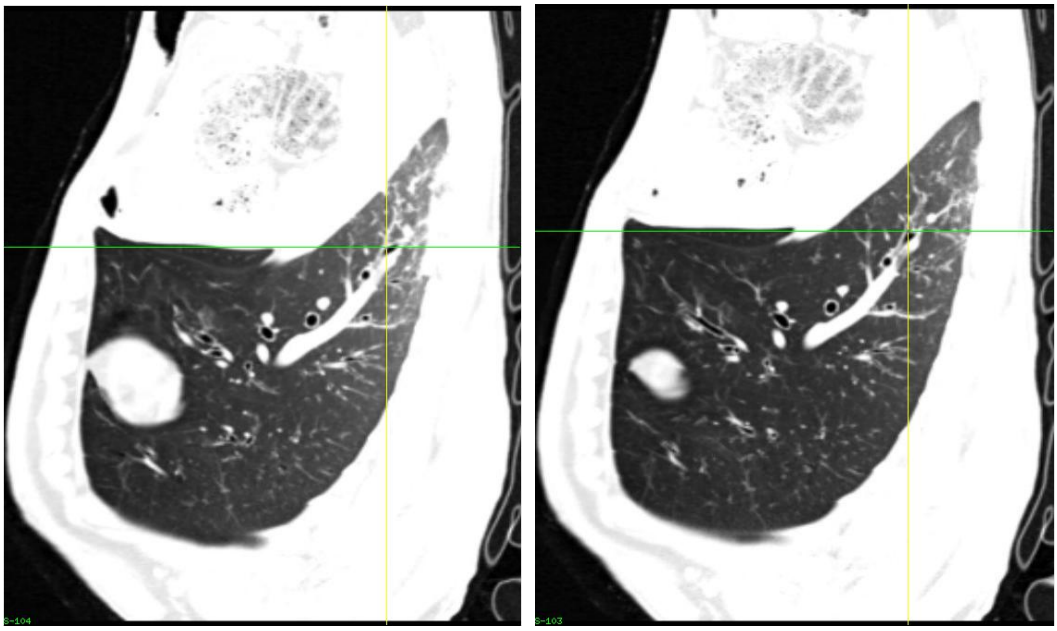

(a) (b)

Figure 3.4: Sagittal view of the landmark position that shows largest registration error in (a) P10 and (b) P15.

3.1.2 Landmark Errors from Manual Reference Standard

In our study, 20 landmarks were manually selected. Figure 3.5 a and b shows the projection of the manually-selected landmark locations onto coronal and sagittal slices for one animal. This figure shows that landmarks are centrally located, with no landmarks in the apices. Figure 3.6 shows the landmark error across seven phase

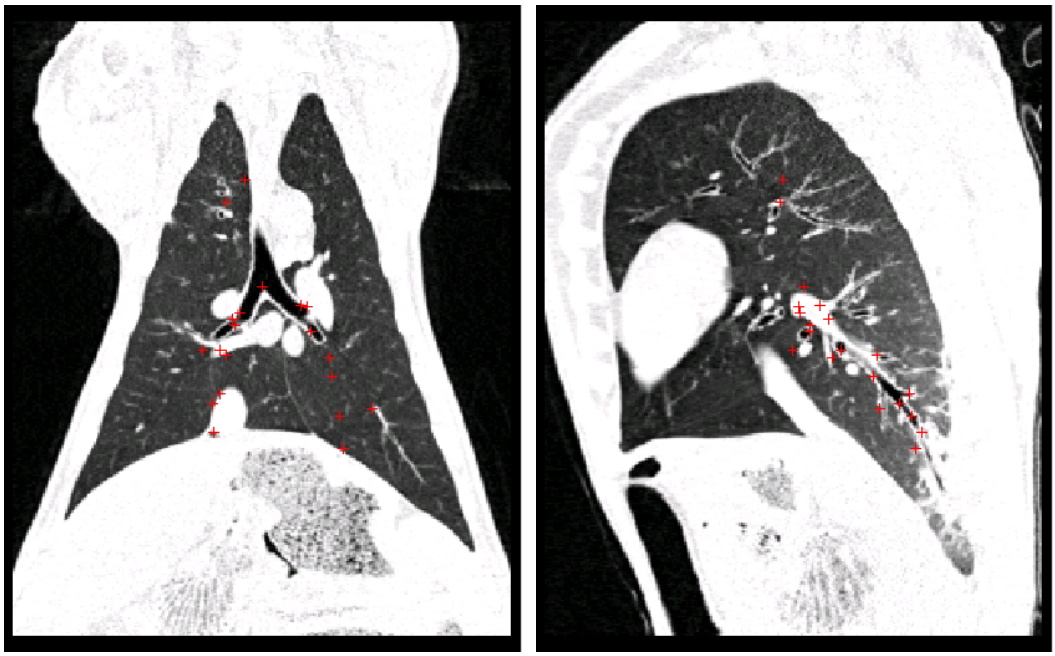

(a) (b)

Figure 3.5: Manually-generated landmark locations projected onto (a) a coronal slice and (b) a sagittal slice for one animal at T0 breathing phase.

change pairs. Overall the registration accuracy is on the order of 1 mm, or about 2 voxels.

Figure 3.7 shows the registration accuracy across three pressure change pairs. We can also see the abnormally large landmark error in pressure change pair P10 to

P15 for animal AS70078 as discussed.

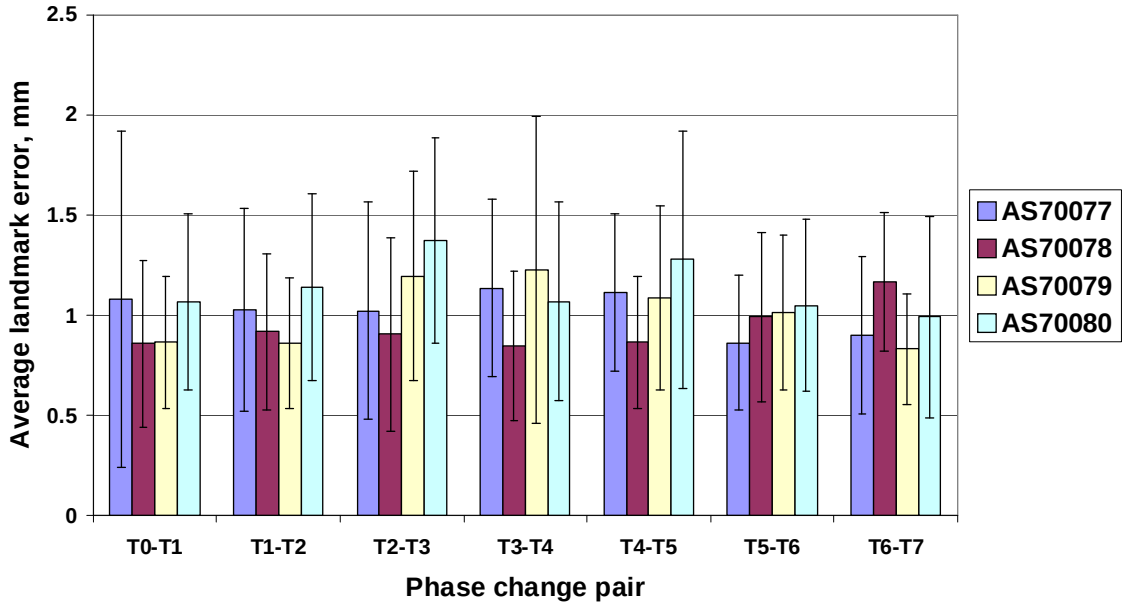

Figure 3.6: Registration accuracy by mean ± standard deviation of landmark errors for each phase change pair and for each animal.

3.1.3 Comparison of Semi-Automatic and Manual Reference Standards

As shown in Figure 3.1 and Figure 3.5, while showing the similar results of landmark errors, the semi-automatic reference has much wider range of landmarks in which registration performance in the whole lung has been evaluated and its assistance to the observer to identify the landmarks shows promising application in quantitative evaluation of registration accuracy. With tracking 200 widely distributed landmarks, we can also see the relationship of landmark error and their locations as shown in Figure 3.8. The landmark error is normal distributed along y axis.

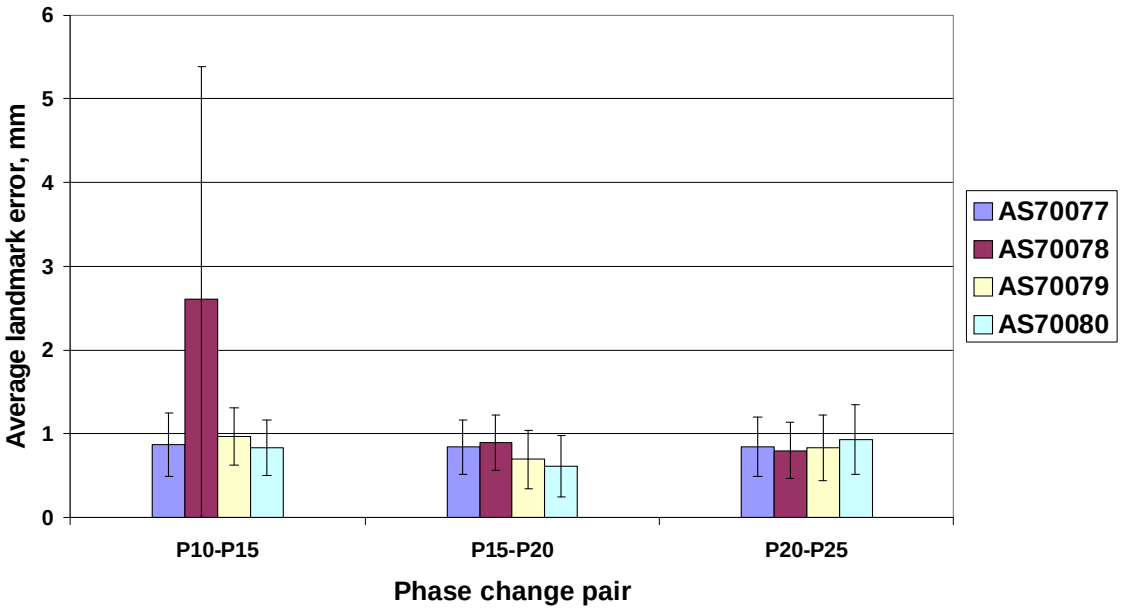

Figure 3.7: Registration accuracy by mean ± standard deviation of landmark errors for each pressure change pair and for each animal.

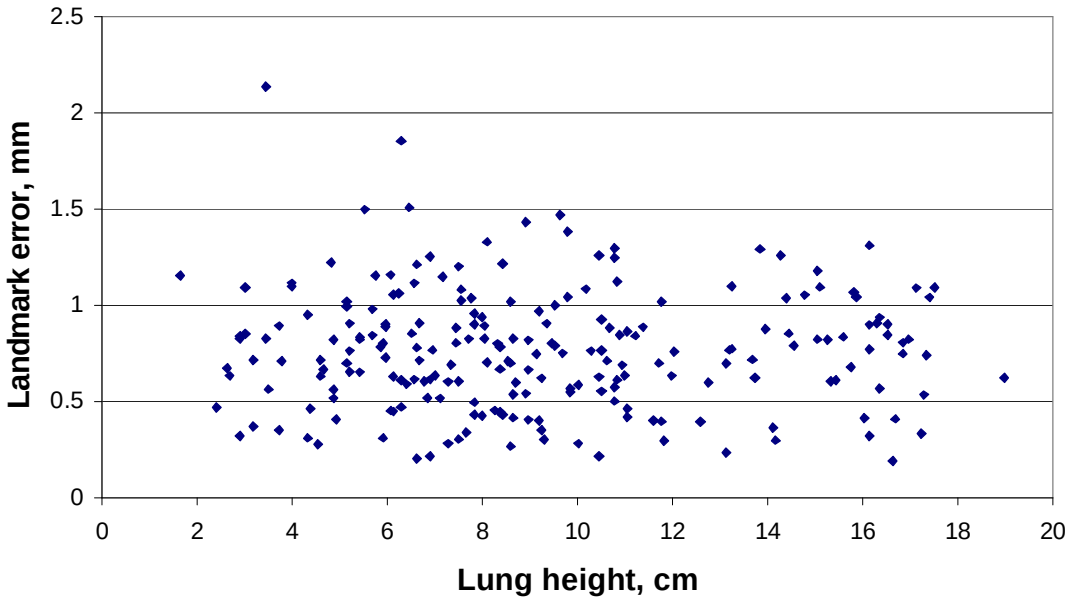

Figure 3.8: Landmark error versus lung height for pressure change pair P10 to P15 in animal AS70080.

20 anatomic landmarks picked manually at the airway branchpoints were also matched automatically across scans. The distance between the automatically matched landmark and the manually matched landmark is shown in Table 3.1.

Landmark ID	P15	P20	P25	Average
1	0.89	0.50	1.05	0.81
2	0.89	0.74	0.89	0.84
3	0.50	0.74	0.74	0.66
4	0.74	0.74	1.58	1.02
5	0.50	0.55	0.55	0.53
6	0.00	0.74	0.74	0.49
7	0.74	0.55	1.05	0.78
8	0.74	0.00	0.00	0.25
9	0.89	1.05	1.65	1.20
10	0.50	0.55	0.92	0.65
11	0.00	1.56	0.89	0.82
12	0.92	0.55	0.55	0.67
13	0.00	0.55	0.50	0.35
14	0.89	0.00	0.50	0.46
15	0.74	1.05	1.65	1.15
16	0.74	0.00	0.55	0.43
17	1.05	0.00	0.92	0.65
18	0.74	0.55	0.55	0.61
19	0.74	0.74	0.74	0.74
20	0.89	0.89	0.89	0.89

Table 3.1: An example of the distance between the automatically matched landmark and the manually matched landmark in differen pressure for animal AS70078.

3.2 Regional Lung Expansion and Xe-CT Estimates of sV

From the registration results and Xe-CT analysis, Jacobian and specific ventilation were calculated, respectively. Color-coded Jacobian map and sV map at approximately the same anatomic location for a sheep are shown in Figure 3.9. From

the two maps, a relationship between the two measurements can be observed.

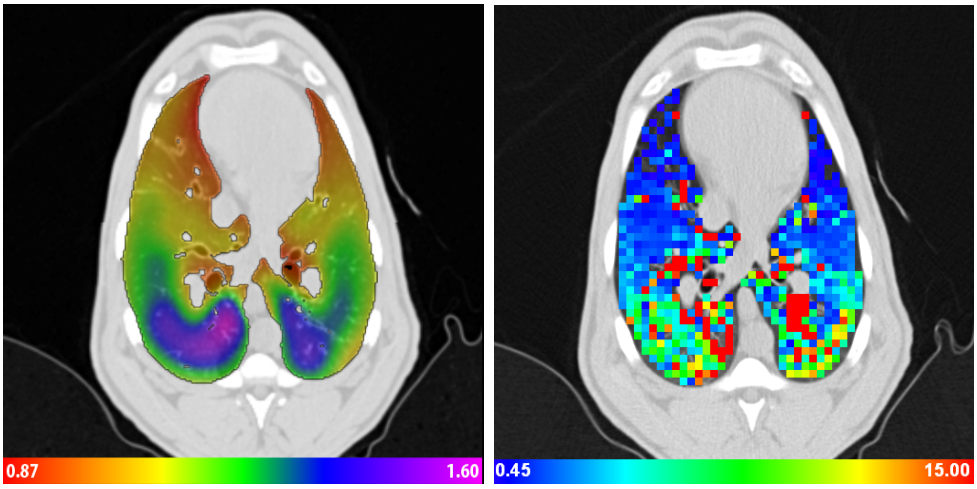

(a) (b)

Figure 3.9: Color-coded maps showing (a) Jacobian of the registration transformation and (b) specific ventilation (1/min) for approximately the same anatomic slice computed from the $P10 - P15$ image pair of the same sheep. Note that the physical units and color scales are different for (a) and (b).

3.2.1 Estimate of Regional Lung Expansion in Dynamic Scans

Figure 3.10a shows the average Jacobian vs. lung height for all phase change pairs. Figure 3.10b shows the average sV vs. lung height calculated from the Xenon-CT study. Both figures show the expected ventralCdorsal gradient in lung expansion and ventilation which is caused by more blood flow in the dorsal regions than the ventral regions [10]. Figure 3.11 shows average Jacobian vs. average sV at the $T0$ to $T1$ inspiration phase change pair and $T4$ to $T5$ expiration phase change pair. The figure gives the equation of the linear regression line with r^2 values and 95% confidence for the linear fits between average sV and the average Jacobian. Figure 3.12 shows

the correlation coefficients r^2 from the linear regression of average Jacobian and sV for each phase change pair and each animal. The phase change pair $T2$ to $T3$ shows the highest average correlation $r^2 = 0.85$ among all phase change pairs.

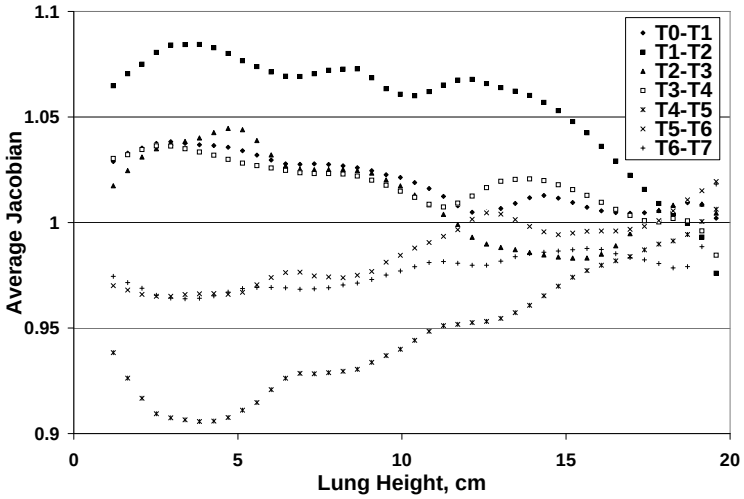

(a)

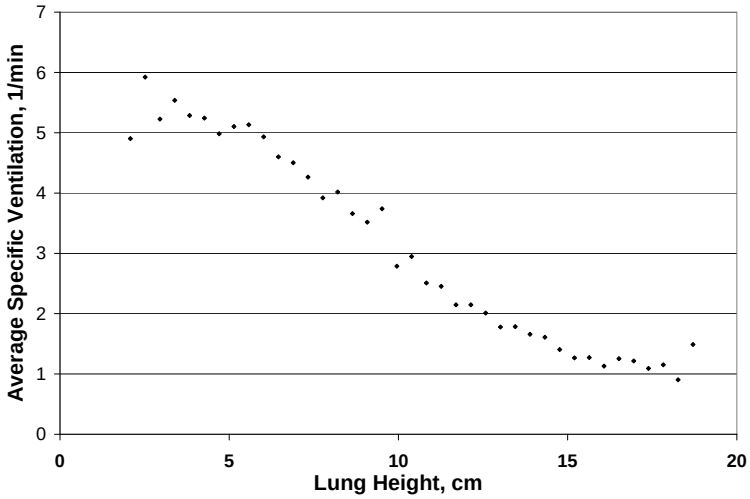

(b)

Figure 3.10: Example of Jacobian and sV measurements vs. lung height for one animal AS70078. (a) Average Jacobian values for all phase change pairs. (b) Average sV vs. lung height. Lung height equal to 0 cm is the most dorsal position and positive heights move toward the ventral direction.

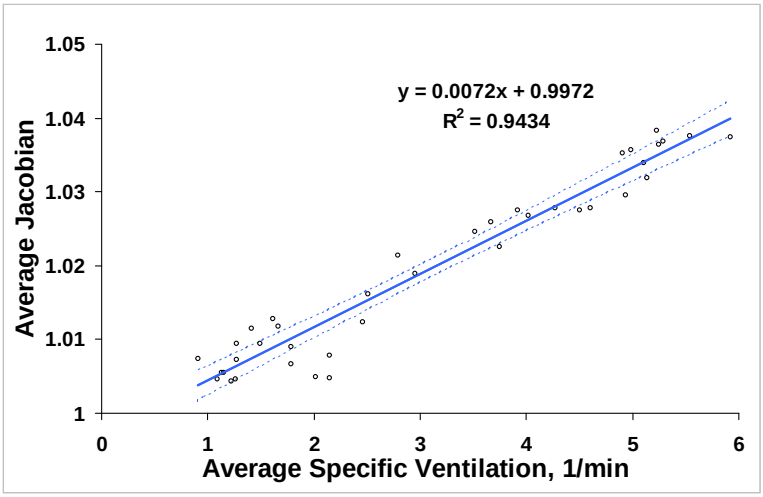

(a)

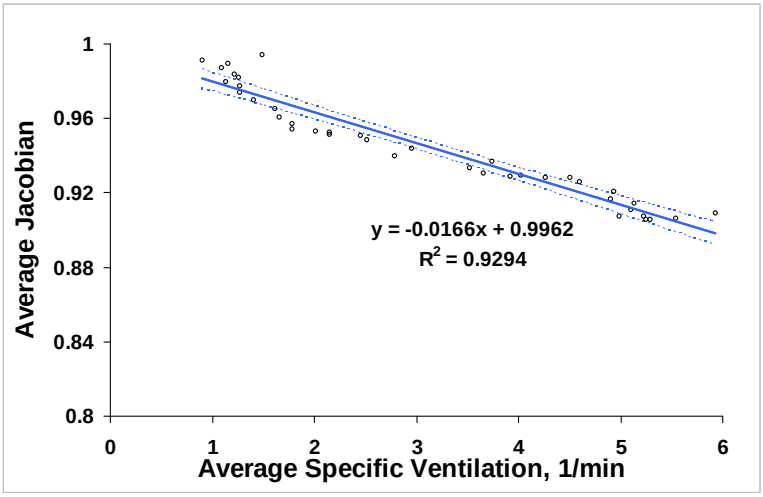

(b)

Figure 3.11: Examples of scatter plot of average sV and average Jacobian for one animal AS70078 with linear regression with 95% confidence interval for (a) $T0$ to $T1$ phase change pair and (b) $T4$ to $T5$ phase change pair.

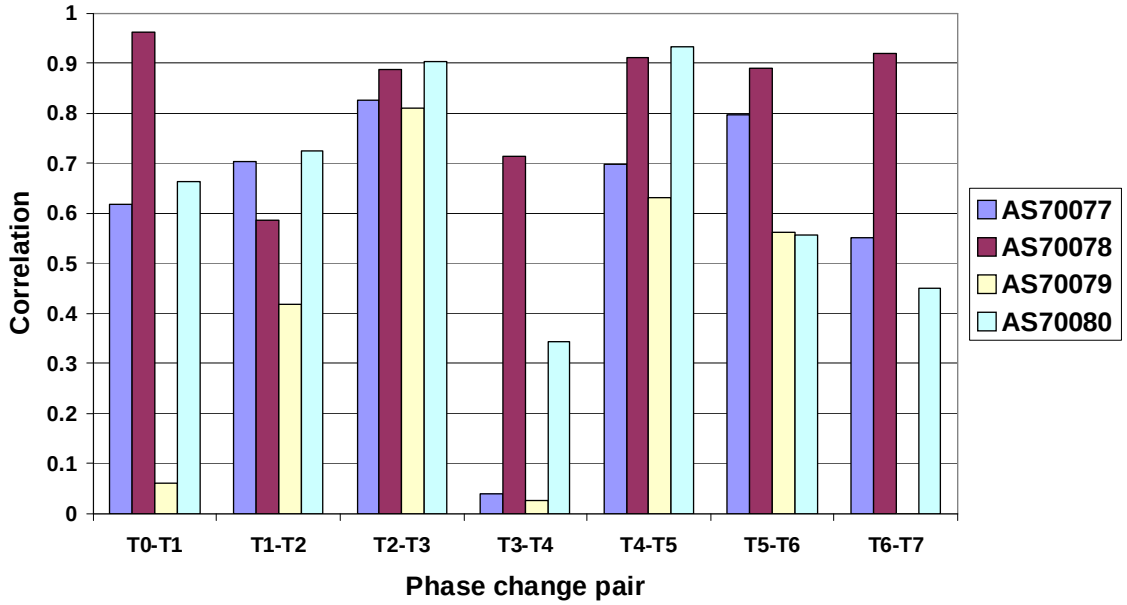

Figure 3.12: Correlation coefficients r^2 from the linear regression of average Jacobian and sV for each phase change pair and for each animal.

3.2.2 Estimate of Regional Lung Expansion in Static Scans

Figure 3.13 shows the correlation coefficients r^2 from the linear regression of average Jacobian and sV for each pressure change pair and each animal. The phase change pair $P20$ to $P25$ shows the highest average correlation $r^2 = 0.84$ among all pressure change pairs.

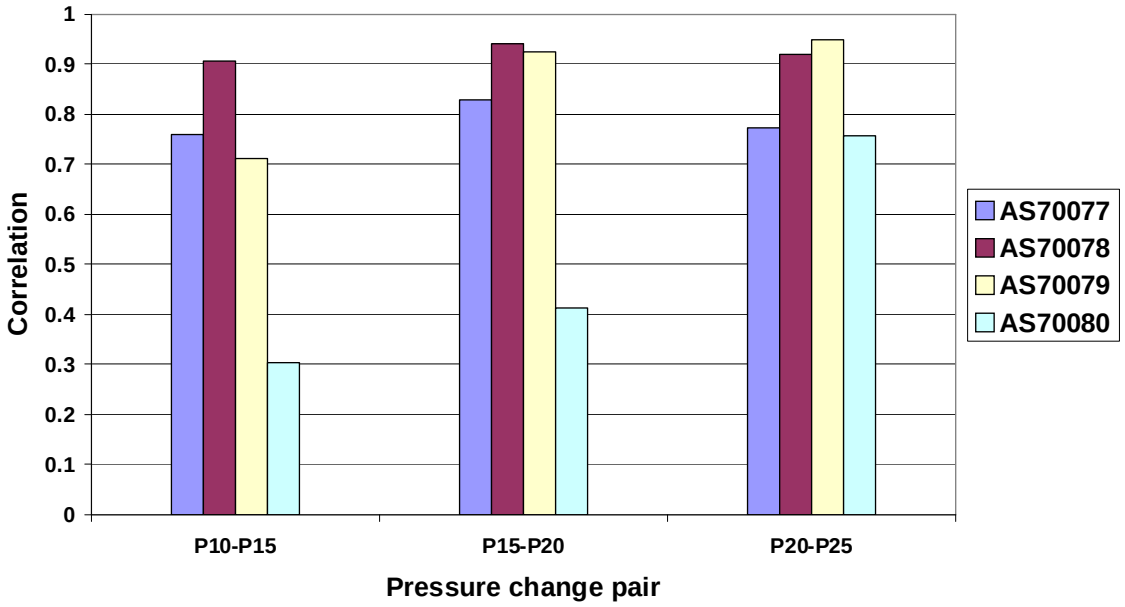

Figure 3.13: Correlation coefficients r^2 from the linear regression of average Jacobian and sV for each pressure change pair and for each animal.

CHAPTER 4
DISCUSSION

4.1 Image Registration

In the introduction of the inverse consistent linear elastic image registration described in Section 2.2.2, we mentioned that the registration algorithm is based on the elastic model which is also our assumption of the mechanical property of the lungs. As we pointed out in Section 2.2.1, because of the assumption of linear elasticity, the registration based on the elastic model is only applicable to small deformations and may fail when recovering large image differences. Though in Section 3.1 we have shown small landmark errors (less than 2 mm), it is our interest to know the relationship between the landmark errors and difference of the input images or in other words, the pressure change in our experiments. Since our objective is to translate our methods for use with humans, it would be necessary to know the limitations of the registration algorithm by more experiments. In current clinical diagnosis, the patient is usually scanned at two different lung volumes - functional residual capacity (FRC) and total lung capacity (TLC). Because of the large anatomic difference between these two scans, whether the basic assumption that the lung as an elastic body still holds true, remains under further investigation. Certainly, the registration model can be replaced by other models. Fluid model, which allows large deformation, can be applied to the cases in which the lungs expand or contract non-elastically when large anatomical difference appears. Figure 3.9 shows the color-coded Jacobian map and sV map at approximately the same anatomic location for a sheep. While the sV map shows strong transition between adjacent anatomical structures such as the airway

and the vessel, the Jacobian value along the boundary is smoothed possibly due to the strong linear elastic constraint [8, 7] used to ensure that the transformations maintain the topology of the images. In contrast, finite element models allow more principled control of localized deformations. With the available image segmentation algorithms for lung, airway tree and vascular tree [17, 2, 33], finite element models which assign to these anatomical structures a local physical description may have more principled control of localized deformations and therefore the mechanical analysis can generate more accurate results than the linear elastic model.

Another issue in registration is the similarity measure C_{SIM} in the equation 2.1. The use of similarity measure such as mean squared intensity leads to the assumption that point intensity is conserved from one image to another, but at different locations. This intensity conservation assumption is globally valid for each volume element outside the lungs because images are of the same modality. However, it is invalid inside the lung where the quantity of inspired air leads to a decrease of lung density as shown in Figure 4.1. Therefore, using the mean squared intensity as the similarity measure alone without further rectification may result in errors in registration. This problem might be solved by changing the similarity measure to other metric such as the mutual information (MI), which is widely used in inter-modality registration [40, 26], by the A *priori* Lung Density Modification technique (APLDM) [32]. We can propose a more complex metric by combining the difference of both intensity change as the measure of the density change and the Jacobian as a measure of volume hcange. The product of these two changes as "tissue weight change" should be conserved during the registration of two lung images since no more matters are added to lungs except air.

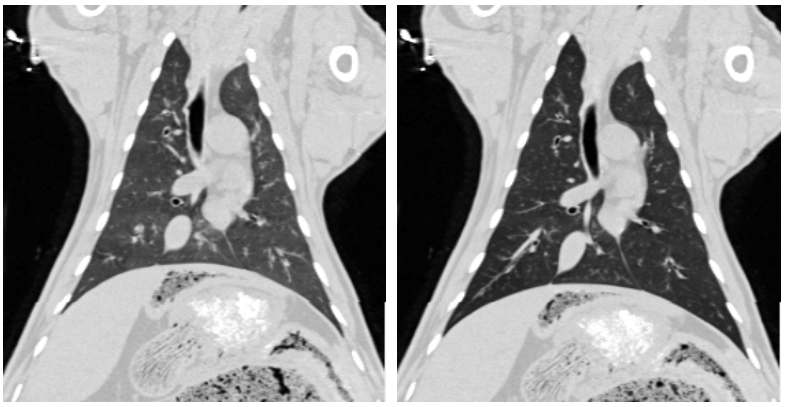

(a) (b)

Figure 4.1: Intensity difference of the lung after inspiration of air. (a) a slice of $P0$ image. (b) a slice of $P10$ image.

4.2 Lung Mechanical Changes During Tidal Breathing

We have calculated estimates of lung expansion from the Jacobian of the registration deformation field during tidal breathing for respiratory phase change pairs. The Jacobian values were compared to the Xe-CT based measures of specific ventilation. The correlation to the Xe-CT sV is equally high in the Jacobian calculated from the dynamic retrospectively reconstructed images ($r^2 = 0.85$) and from the static breath-hold images ($r^2 = 0.84$) as we reported in Section 3.2. Since the Xe-CT data is collected over several breaths during tidal breathing, it is reasonable to expect that the Jacobian calculated from the dynamic scans would more closely reflect the ventilation patterns measured by the Xe-CT. However, the results do not prove our preassumptions. It might be caused by the relatively small and close pressure difference in the static scans so that those scans are at similar airway pressure level as the dynamic scans in tidal breathing. Further investigation of the pressure measurement for the dynamic scans during the tidal breathing is needed.

Even though the comparison of the Jacobian to the sV shows equally good result in both dynamic scans and static scans in the terms of correlation coefficient, the true dynamics of the respiratory system are probably better revealed using dynamic scans acquired across free breathing since the moving lungs have mass, inertia, and hysteresis. Figure 4.2 and Figure 4.3 show the different phases change pair for different regions of the lung when largest expansion and contraction occur. Most of the lung regions will have the largest expansion at the middle phase ($T1$ to $T2$ or 25% to 50% of the inspiration duration) and the largest contraction at the beginning phase ($T4$ to $T5$ or 100% to 75% of the expiration duration). The color coded regions show that the lung does not expand or contract uniformly along the phases. It would be interesting to determine if the regions will shift with different position and level of inspiration. More experiments would need to be designed to decide whether the regions depend on two or more factors. The motion hysteresis, which is patient specific, can be revealed by tracking individual points using the deformation filed across dynamic scans as shown in Figure 4.4.

4.3 Limitations and Future Improvements

Like other registration-based lung functional imaging analysis, the proposed approaches have few apparent limitations. One is the time cost of the 3D image registration. Even working on a workstation with dual Intel Xeon 2.33GHz processors and 16 GB of RAM, the 3D registration of one image pair took an average of 40 to 50 minutes. The relatively long computational time will limit its clinical application if no further improvement regarding time cost is achieved. However, recently there is a promising technique to translate the registration problem into a linear programming

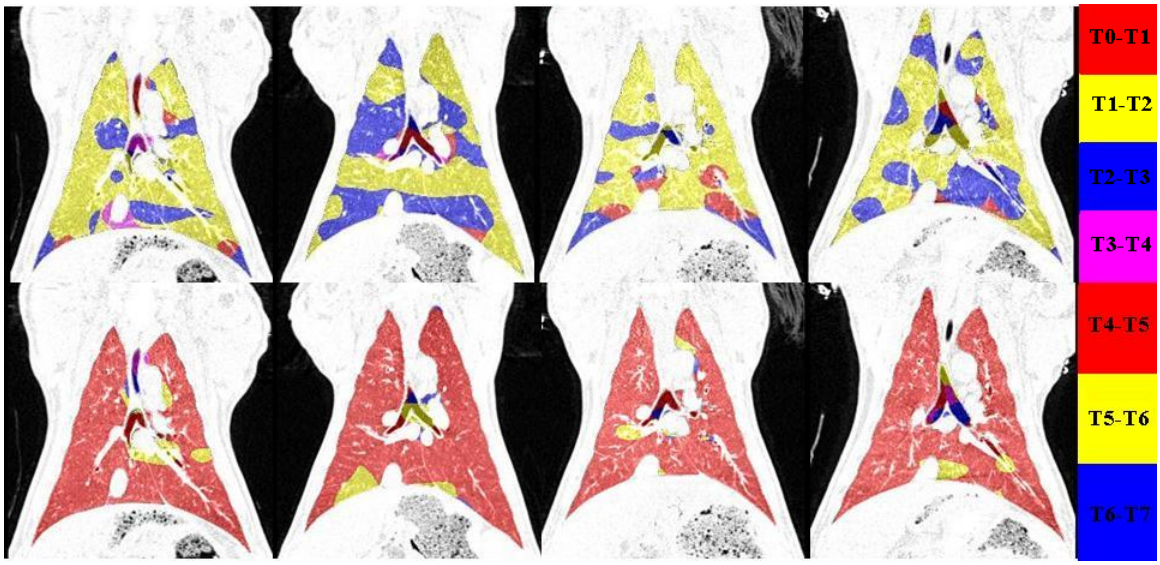

Figure 4.2: Color coded image showing coronal view of the the phase change pair when the largest expansion occurs during inspiration(first row) and the largest contraction occurs during expiration(second row). From left to right: Sheep AS70077, AS70078, AS70079 and AS70080.

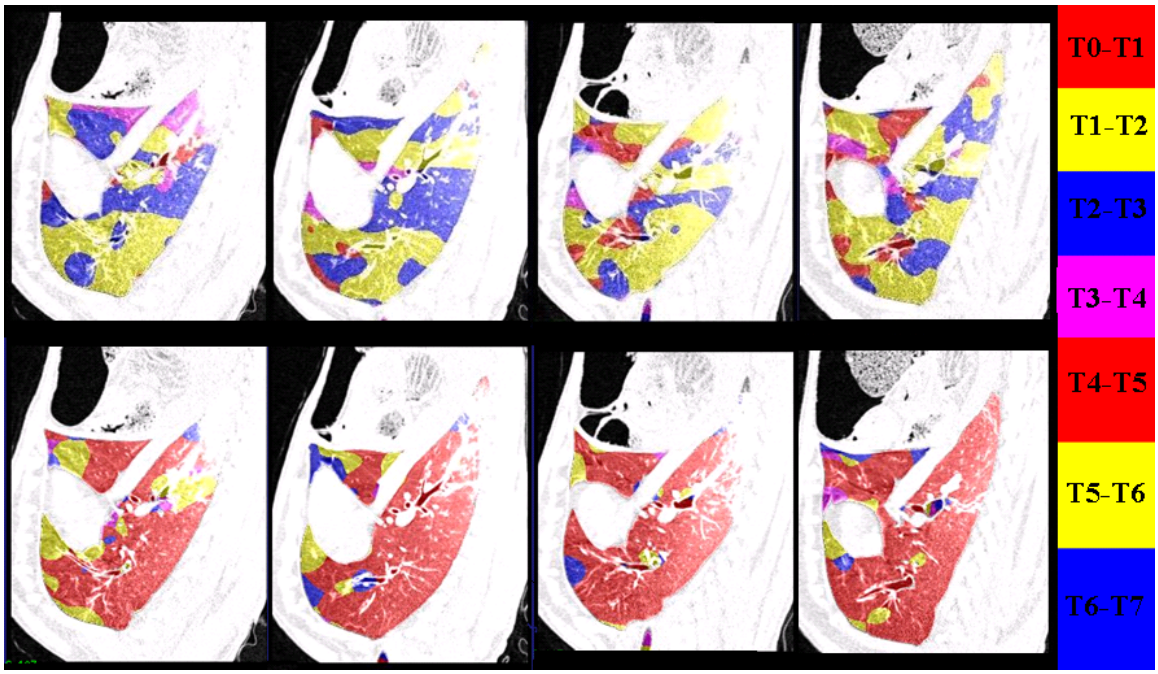

Figure 4.3: Color coded image showing sagittal view of the phase change pair when the largest expansion occurs during inspiration(first row) and the largest contraction occurs during expiration(second row). From left to right: Sheep AS70077, AS70078, AS70079 and AS70080.

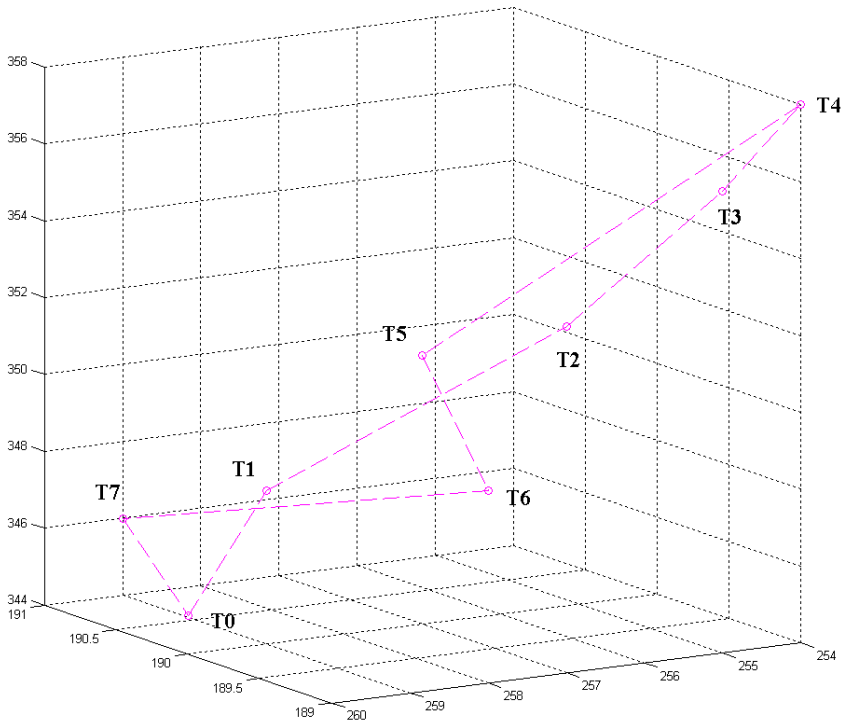

Figure 4.4: An example of the motion hysteresis of a point near diaphragm of sheep AS70078 during tidal breathing.

problem [12] and reduces the computational time from hours to several minutes. The other limitation is the registration accuracy that depends on the model and the similarity measure. As discussed in Section 4.1, the linear elastic model used in our registration algorithm is based on the assumption that the lung is an elastic body. Also our similarity measure does not take into consideration the intensity decrease with inspired air. The accuracy of the registration will directly affect our resolution of the Jacobian map and mechanical analysis, hence more experiments should be done to validate the registration and improve the accuracy whenever necessary before translation for use in humans. Finally, for imaging humans during normal respiration, the dynamic scans may pose some challenges. The retrospectively reconstructed respiratory-gated images require regular and repeatable breathing patterns, so the

subject must be trained to breath properly before images are acquired. In addition, since image data is gathered over several breaths and then reconstructed at different phases, the dynamic imaging will deliver more radiation dose than a single pair of breath-hold scans. Low dose imaging and/or *prospective* respiratory-gating may be able to reduce the radiation exposure. With the validation of the best correlated phase change pair during tidal breathing, the subject will only need to be scanned at two certain phases and the radiation dose will be significantly reduced.

In order to eliminate above limitations, future work will be done to improve the registration model and metric if the registration does not work equally well as shown in animal data when applied to humans. More research is required to determine how the image acquisition protocol can be modified for use in humans and how the increased noise might affect the image registration if we use low dose scans. Since our long-term objective of this research is to utilize high-resolution maps of regional lung mechanical properties to detect and follow the progression of lung disease, more work needs to be done to compare the normal lung and diseased lung. Study of the mechanical properties and indexes such as the Jacobian and strain will be necessary for establishing a functional atlas of the normal lung by applying the inter-subject image registration.

CHAPTER 5
CONCLUSION

We have described a technique that uses multiple respiratory-gated CT images of the lung acquired at different levels of inflation with both breath-hold static imaging and retrospectively reconstructed dynamic imaging, along with non-rigid 3D image registration, to make local estimates of lung tissue expansion. We have compared these lung expansion estimates to Xe-CT derived measures of regional ventilation to validate our measurements. The correlation to the Xe-CT sV is equally high in the Jacobian calculated from the dynamic retrospectively reconstructed images ($r^2 = 0.85$) and from the static breath-hold images ($r^2 = 0.84$). Our semi-automatic reference standard and manual reference standard to quantitatively evaluate the accuracy of 3D image registration have indicated that the average registration error is less than 2 mm. The ability to estimate regional expansion maps as a surrogate of the Xe-CT ventilation imaging for the entire lung, from quickly and easily obtained respiratory-gated images, is a significant contribution to functional lung imaging because of the potential increase in resolution, and large reductions in imaging time, radiation, and contrast agent exposure. If these methods can eventually be extended to humans, they would provide important new tools for studying the lung. Xe-CT requires the use of expensive xenon gas and the associated hardware to control delivery of the gas and harvest the gas from expired air for recycling. In addition, it is known that xenon gas has a strong anesthetic effect that must be carefully monitored. Finally, Xe-CT imaging protocols require high temporal resolution imaging, so typically axial coverage is limited to just a few slices at a time. However, if a registration-based

analysis of easy-to-acquire volumetric images at two different volumes by either static or dynamic scans could be registered, high-resolution maps of lung expansion could be produced for the entire lung with low cost and dose.

REFERENCES

[1] Y. Amit. A non-linear variational problem for image matching. *SIAM Journal on Scientific Computation*, 15(1):207–224, January 1994.

[2] Deniz Aykac, Eric A. Hoffman, Geoffrey McLennan, and Joseph M. Reinhardt. Segmentation and analysis of the human airway tree from three-dimensional X-ray CT images. *IEEE Trans. Medical Imaging*, 22(8):940–950, Aug. 2003.

[3] Deokiee Chon, Kenneth C. Beck, Brett A. Simon, Hidenori Shikata, Osama I. Saba, and Eric A. Hoffman. Effect of low-xenon and krypton supplementation on signal/noise of regional CT-based ventilation measurements. *J. Applied Physiology*, 102:1535–1544, 2007.

[4] Deokiee Chon, Brett A. Simon, Kenneth C. Beck, Hidenori Shikata, Osama I. Saba, Chulho Won, and Eric A. Hoffman. Differences in regional wash-in and wash-out time constants for xenon-CT ventilation studies. *Respiratory Physiology & Neurobiology*, 148:65–83, 2005.

[5] Gary E. Christensen, J. H. Song, W. Lu, I. El Naqa, and D. A. Low. Tracking lung tissue motion and expansion/compression with inverse consistent image registration and spirometry. *Med Physics*, 34(6):2155–2165, June 2007.

[6] G.E. Christensen and H.J. Johnson. Consistent image registration. *IEEE Trans. Med. Imaging*, 20(7):568–582, July 2001.

[7] G.E. Christensen, S.C. Joshi, and M.I. Miller. Volumetric transformation of brain anatomy. *IEEE Trans. on Med. Imaging*, 16(6):864–877, December 1997.

[8] G.E. Christensen, R.D. Rabbitt, and M.I. Miller. 3D brain mapping using a deformable neuroanatomy. *Physics in Medicine and Biology*, 39:609–618, 1994.

[9] W R Crum and T Hartkens. Non-rigid image registration: theory and practice. *British Journal of Radiology*, 77(S):140–153, 2004.

[10] I. Galvin, G. B. Drummond, and M. Nirmalan. Distribution of blood flow and ventilation in the lung: gravity is not the only factor. *Br. J. Anaesth.*, page aem036, 2007.

[11] James Gee, Tessa Sundaram, Ichiro Hasegawa, Hidemasa Uematsu, and Hiroto Hatabu. Characterization of regional pulmonary mechanics from serial magnetic resonance imaging data. *AR*, 10:1147–1152, 2003.

[12] Ben Glocker, Nikos Komodakis, Georgios Tziritas, Nassir Navab, and Nikos Paragios. Dense image registration through mrfs and efficient linear programming. *Medical Image Analysis*, In press.

[13] Thomas Guerrero, Kevin Sanders, Edward Castillo, Yin Zhang, L. Bidaut, and T. Pan R. Komaki. Dynamic ventilation imaging from four-dimensional computed tomography. *Phys Med Biol.*, 51(4):777–791, Feb. 21 2006.

[14] Thomas Guerrero, Kevin Sanders, Josue Noyola-Martinez, Edward Castillo, Yin Zhang, Richard Tapia, Rudy Guerra, Yerko Borghero, and Ritsuko Komaki. Quantification of regional ventilation from treatment planning CT. *Int. J. Radiation Oncology Biol. Phys.*, 62(3):630–634, Jul 1 2005.

[15] E. A. Hoffman, T. Behrenbeck, P. A. Chevalier, and E. H. Wood. Estimation of pleural surface expansile forces in intact dogs. *J. Applied Physiology*, 55(3):935–948, Sept. 1983.

[16] Eric A. Hoffman and Edwin van Beek. Hyperpolarized media mr imaging - expanding the boundaries? *Academic Radiology*, 13(8):929–931, 2006.

[17] Shiying Hu, Eric A. Hoffman, and Joseph M. Reinhardt. Automatic lung segmentation for accurate quantitation of volumetric X-ray CT images. *IEEE Trans. Medical Imaging*, 20(6):490–498, June 2001.

[18] R. Hubmayr, B. Walters, P.A. Chevalier, J.R. Rodarte, and L.E. Olson. Topographical distribution of regional lung volume in anesthetized dogs. *J. Applied Physiology*, 54(4):1048–1056, 1983.

[19] Luis Ibanez, William Schroeder, Lydia Ng, and Josh Cates. *The ITK Software Guide*. Kitware, Inc, 2005.

[20] Hans J. Johnson. Method for consistent linear-elastic medical image registration. Master's thesis, Department of Electrical and Computer Engineering, The University of Iowa, Iowa City, IA 52242, May 2000.

[21] H.J. Johnson and G.E. Christensen. Consistent landmark and intensity-based image registration. *IEEE Trans. Med. Imaging*, 21(5):450–461, 2002.

[22] H. Lester and S.R. Arridge. A survey of hierarchical non-linear medical image registration. *Medical Image Analysis*, 32(1):129–149, 1999.

[23] Visualizing lung function with positron emission tomography. R. scott harris and daniel p. schuster. *Journal of Applied Physiology*, 102, 2007.

[24] J.B.A. Maintz and M.A. Viergever. A survey of medical image registration. *Medical Image Analysis*, 2(1):1–36, 1998.

[25] C Marcucci, D Nyhan, and B A Simon. Distribution of pulmonary ventilation using Xe-enhanced computed tomography in prone and supine dogs. *JAP*, 90(2):421–430, 2001.

[26] D. Mattes, D.R. Haynor, H. Vesselle, T.K. Lewellen, and W. Eubank. Pet-ct image registration in the chest using free-form deformations. *IEEE Transactions on Medical Imaging*, 22(1):120–128, Jan. 2003.

[27] Harald E. Moller, X. Josette Chen, Brian Saam, Klaus D. Hagspiel, G. Allan Johnson, Talissa A. Altes, Eduard E. de Lange, and Hans-Ulrich Kauczor. MRI of the lungs using hyperpolarized noble gases. *Magnetic Resonance in Medicine*, 47(6):1029–1051, 2002.

[28] K. Murphy, B. van Ginneken, J.P.W. Pluim, S. Klein, and M. Staring. Semi-automatic reference standard construction for quantitative evaluatoin of lung ct registration. In *Proc. of International Conference on Medical Image Computing and Computer-Assisted Intervention 2008*, In Press.

[29] P.C. Pratt. *Emphysema and chronic airways disease*, pages 654–659. Springer-Verlag, 1998. edited by D. Dail and S. Hammar.

[30] Joseph M. Reinhardt, Kai Ding, Kunlin Cao, Gary E. Christensen, Eric A. Hoffman, and Shalmali V. Bodas. Registration-based estimates of local lung tissue expansion compared to xenon-ct measures of specific ventilation. *Medical Image Analysis*, In press.

[31] H T Robertson, R W Glenny, D Stanford, L M McInnes, D L Luchtel, and D Covert. High-resolution maps of regional ventilation utilizing inhaled fluorescent microspheres. *J. Applied Physiology*, 82(3):943–953, 1997.

[32] David Sarrut, Vlad Boldea, Serge Miguet, and Chantal Ginestet. Simulation of four-dimensional ct images from deformable registration between inhale and exhale breath-hold ct scans. *Medical Physics*, 33(3):605–617, 2006.

[33] Hidenori Shikata, Eric A. Hoffman, and Milan Sonka. Automated segmentation of pulmonary vascular tree from 3d ct images. volume 5369, pages 107–116. SPIE, 2004.

[34] B A Simon and C Marcucci. Parameter estimation and confidence intervals for Xe-CT ventilation studies: A Monte Carlo approach. *JAP*, 84(2):709–716, 1998.

[35] Tessa A. Sundaram and James C. Gee. Towards a model of lung biomechanics: pulmonary kinematics via registration of serial lung images. *Medical Image Analysis*, 9(6):524–537, 2005.

[36] J. K. Tajik, D. Chon, C.-H. Won, B. Q. Tran, and E. A. Hoffman. Subsecond multisection CT of regional pulmonary ventilation. *AR*, 9:130–146, 2002.

[37] Martin Urschler, Stefan Kluckner, and Horst Bischof. A framework for comparison and evaluation of nonlinear intra-subject image registration algorithms. In *ISC/NA-MIC Workshop on Open Science at MICCAI 2007*, 2007.

[38] Edwin J.R. van Beek, Jim M. Wild, Hans-Ulrich Kauczor, Wolfgang Schreiber, John P. Mugler III, and Eduard E. de Lange. Functional MRI of the lung using hyperpolarized 3-helium gas. *Journal Of Magnetic Resonance Imaging*, 20(4):550–554, 2004.

[39] Jose G. Venegas, Tilo Winkler, Guido Musch, Marcos F. Vidal Melo, Dominick Layfield, Nora Tgavalekos, Alan J. Fischman, Ronald J. Callahan, Giacomo Bellani, and R. Scott Harris. Self-organized patchiness in asthma as a prelude to catastrophic shifts. *Nature*, 7034(2-3):777–782, 2005.

[40] P. Viola and W. M. Wells III. Alignment by maximization of mutual information. *International Journal of Computer Vision*, 24(2):137–154, 1997.

[41] Chulho Won, Deokiee Chon, Jehangir Tajik, Binh Q. Tran, G. Blake Robinswood, Kenneth C. Beck, and Eric A. Hoffman. Ct-based assessment of regional pulmonary microvascular blood flow parameters. *Journal of Applied Physiology*, 94(6):2483–2493, 2003.